PHILOSOPHICAL TRANSACTIONS OF THE ROYAL SOCIETY A
MATHEMATICAL, PHYSICAL & ENGINEERING SCIENCES

Experimental Validation of Condensing Flow Theory for a Stationary Cascade of Steam Turbine Blades

A. J. White, J. B. Young and P. T. Walters

Phil. Trans. R. Soc. Lond. A 1996 **354**, 59-88
doi: 10.1098/rsta.1996.0003

Experimental validation of condensing flow theory for a stationary cascade of steam turbine blades

By A. J. White[1], J. B. Young[1] and P. T. Walters[2]

[1] *Whittle Laboratory, Cambridge University Engineering Department,*
Madingley Road, Cambridge CB3 0DY, UK
[2] *Formerly of National Power Technology and Environmental Centre,*
Kelvin Avenue, Leatherhead, Surrey KT22 7SE, UK

The paper describes a detailed experimental and theoretical study of non-equilibrium condensing steam flow in a stationary cascade of turbine blades operating transonically. Instrumentation was installed for obtaining colour schlieren photographs of the shock wave structure, the blade surface static pressure distribution, the pitchwise variation of the mean droplet radius downstream of the cascade and the stagnation pressure loss across the cascade. Only one blade profile was tested but a comprehensive set of measurements was acquired covering a wide range of inlet steam conditions and exit Mach numbers. By careful interpretation of the data, it was possible, for the first time, to infer the thermodynamic loss due to irreversible condensation directly from experimental measurements. An elaborate comparison of the experimental data with condensing flow theory was also undertaken using a two-dimensional inviscid time-marching calculation scheme, simulating both steady and unsteady flows. Excellent agreement was obtained throughout and it can be stated with some confidence that the theory and calculation procedures used reproduce accurately all the main features of steady transonic condensing flow in stationary cascades.

Roman symbols

E	$e+\frac{1}{2}u^2$
e	specific internal energy
H	$h+\frac{1}{2}u^2$
h	specific enthalpy
h_{fg}	specific enthalpy of evaporation
J	homogeneous nucleation rate per unit mass of mixture
k	Boltzmann's constant
M	Mach number
M_{2s}	Average isentropic Mach number at cascade exit
m	mass of a molecule
n	droplet number per unit mass of mixture
P	static pressure
P_0	total pressure
Pr	Prandtl number
q_c	condensation coefficient

Phil. Trans. R. Soc. Lond. A (1996) **354**, 59–88
Printed in Great Britain

r	droplet radius
r_*	Kelvin–Helmholtz critical radius
s	specific entropy
T	temperature
ΔT_0	cascade inlet stagnation superheat
$\boldsymbol{u}$	flow velocity vector
y	wetness fraction

Greek symbols

λ	thermal conductivity
ρ	density
σ	liquid surface tension
ζ	Markov energy loss coefficient

Subscripts

f	liquid phase
g	vapour phase
i	droplet group-i
s	saturated
0	stagnation (total) condition
1	cascade inlet condition
2	cascade outlet condition

1. Introduction

In the large steam turbines used for electrical power production, the steam enters the low-pressure (LP) turbine cylinders as a dry superheated vapour but exhausts to the condenser as a two-phase mixture of saturated vapour and small liquid droplets. Within the blade passages, the liquid droplets are formed mainly by homogeneous nucleation as the vapour becomes highly supersaturated due to the rapid expansion process. Once formed, the droplets grow rapidly, but the rate of expansion in the blade passages is generally so high that thermodynamic equilibrium is only established in the inter-row gaps and in the final turbine exhaust diffuser leading to the condenser. Departures from equilibrium are manifest by differences in temperature between the droplets and the vapour and by the fact that the wetness fraction of the two-phase mixture differs from the equilibrium value corresponding to the local pressure and entropy. Velocity slip between the phases also occurs but, for the submicron sized droplets which constitute the main bulk of the liquid phase, this is much less significant than the effects of thermal non-equilibrium.

There are two main reasons why departures from thermal equilibrium in steam turbines are important. First, the heat and mass transfer between the vapour and liquid phases can have a strong effect on the flow behaviour within the blade passages. This is particularly marked in the final LP turbine stages where the flow becomes supersonic and generates shock waves which can interact in a most complex way with the processes of droplet nucleation and growth. Second, non-equilibrium condensation is a thermodynamically irreversible process resulting in the production of entropy which, ultimately, translates into a reduction in turbine efficiency. The loss in turbine efficiency due to wetness (of which the thermodynamic effect is an important component) has never been precisely quantified. However, the empirical Baumann 'rule of thumb', universally adopted by turbine designers to model the loss in calculation procedures, suggests that its effect is comparable to, or even greater than, the conventional viscous losses.

Since the privatization of the electricity generating industry in the United Kingdom, there has been a rapid swing in fashion away from the large steam-based coal-fired power plants formerly favoured by the Central Electricity Generating Board towards smaller, but more efficient, 'combined cycle' plants utilizing natural gas as the fuel (Horlock 1993). The combined cycle comprises a gas turbine cycle topping a steam cycle and it is interesting to note that current design procedures often specify a steam wetness at turbine exhaust which is considerably higher than that associated with the older plants (12–15% as opposed to 8–10%). Potentially, the problems of wetness are now technically more important than ever before.

The computation of condensing flows poses many problems which do not arise in single-phase calculations. Foremost amongst these is the need to specify mathematical models for droplet nucleation and condensation and to devise techniques for the stable and accurate numerical solution of the resulting equations simultaneously with the conservation equations of mass, momentum and energy. Difficulties arise because the droplet spectrum is polydispersed and it is usually necessary to compute the behaviour of a large number of droplet groups to represent, in a discrete fashion, the real continuous droplet size distribution. Nevertheless, much progress has been made in the analysis of vapour-droplet flows. Two-dimensional steady-flow calculation procedures have been reported for pure steam by Bakhtar & So (1991) and by Young (1992), and for moist air by Schnerr & Dohrmann (1988). Recently, a calculation procedure for the two-dimensional unsteady flow of condensing steam has been devised by White & Young (1993) and it is this approach which has been used for the calculations described below.

Progress in experimentation has been less satisfactory. Wet-steam is a difficult medium in which to obtain measurements and most of the data used for validation purposes have been obtained in simple one-dimensional nozzle experiments (Young 1982). Initially, the only measurements technically possible were of the axial static pressure distribution through the (misleadingly named) 'condensation shock', but these provided insufficient data to fix empirically the unknown parameters in the theoretical models. Subsequently, a great advance in instrumentation was made by the introduction of an optical technique for measuring the wetness properties (Walters 1973). This has now been developed to such an extent that wetness fraction and mean droplet size data can be obtained, not only in laboratory nozzles, but also in operational machines (Walters 1985). In many cases, the actual number distribution of droplet sizes can also be inferred by numerically inverting the optical transmission data (Walters 1980).

The current situation is that agreement between theory and experiment for steady and periodically oscillating flows in one-dimensional nozzles is generally satisfactory. Almost no experimental data is available, however, for the case of two-dimensional condensing flow in stationary cascades of turbine blades and this is the area addressed by the present paper. For turbomachinery blade design, the stationary linear cascade is one of the most important pieces of test equipment for establishing the validity of new profile geometries and obtaining data on profile loss. For steam turbine blading, almost all of this testing has been performed in air, partly for convenience and partly because the importance of testing in real condensing steam flows was not originally recognized. Testing in steam introduces many extra difficulties associated with contamination of the instrumentation and flow visualization by condensate, and long thermal settling times between condition changes. A novel 'blow down' facility described by Bakhtar *et al.* (1993) goes some way towards overcoming these problems but the small scale of the blading used, coupled with the short times available for measurement, inevitably imposed severe restrictions on the quality of the data obtainable.

In contrast, the investigation described in this paper marks a return to steady flow cascade testing using full-sized blades but, in this case, operated with steam at realistic LP turbine conditions. For the blade profile tested, a comprehensive set of measurements was acquired covering a wide range of operating conditions in terms of inlet superheat and outlet Mach number. Instrumentation was installed for obtaining the blade surface static pressure distribution, colour schlieren photographs of the shock wave structure, the pitchwise variation of the mean droplet diameter and the stagnation pressure loss across the cascade. By careful interpretation of the data, it proved possible, for the first time, to infer the thermodynamic loss due to condensation directly from experimental measurements.

2. Experimental facility and test cascade

The experiments were performed in the wet-steam facility of the National Power Technology and Environmental Centre, Leatherhead (formerly the Central Electricity Research Laboratories). General details of the facility are described by Moore *et al.* (1973) and a preliminary investigation (using a different cascade) is reported by Skillings (1989).

Steam was supplied to the test section (shown in figure 1) from two 1.5 MW boilers via an electrical superheater and a single-stage impulse turbine. The steam condition at inlet to the test section could be varied from a wet equilibrium to a superheated state by adjusting the speed of the turbine. The flow leaving the test section was passed to a condenser via an adjustable duct. By varying the cooling water flow rate in the condenser, the test section pressure ratio, and hence the exit Mach number, could be controlled. However, for most tests, the exit flow condition was controlled by varying the upper tailboard angle on the cascade (see below) with the condenser pressure being maintained at its minimum value.

With reference to figure 1, steam entered the test section via a converging nozzle and parallel liner which contained channels and bleed slots to remove sidewall condensate. This avoided contamination of the schlieren windows with coarse water, enabling clear visualization of the trailing edge shock waves. The depth of the test section was 152 mm, giving a blade aspect ratio (blade height over axial chord) of 1.55 and ensuring a reasonably two-dimensional flow-field at the mid-plane of the passage.

The turbine blade profile selected for the experiments is shown in figure 2 and was a copy of a fifth stage stator blade from the six-stage LP cylinder of a 660 MW turbine. The design exit Mach number was 1.2 and the outlet flow angle about 71°. This profile was chosen because experiments previously conducted in the actual turbine had indicated high losses in the fifth stage (which also corresponded to the location of the primary nucleation).

Full-sized blade profiles were installed in the test section since scaling down would have resulted in higher expansion rates and thus larger departures from equilibrium.

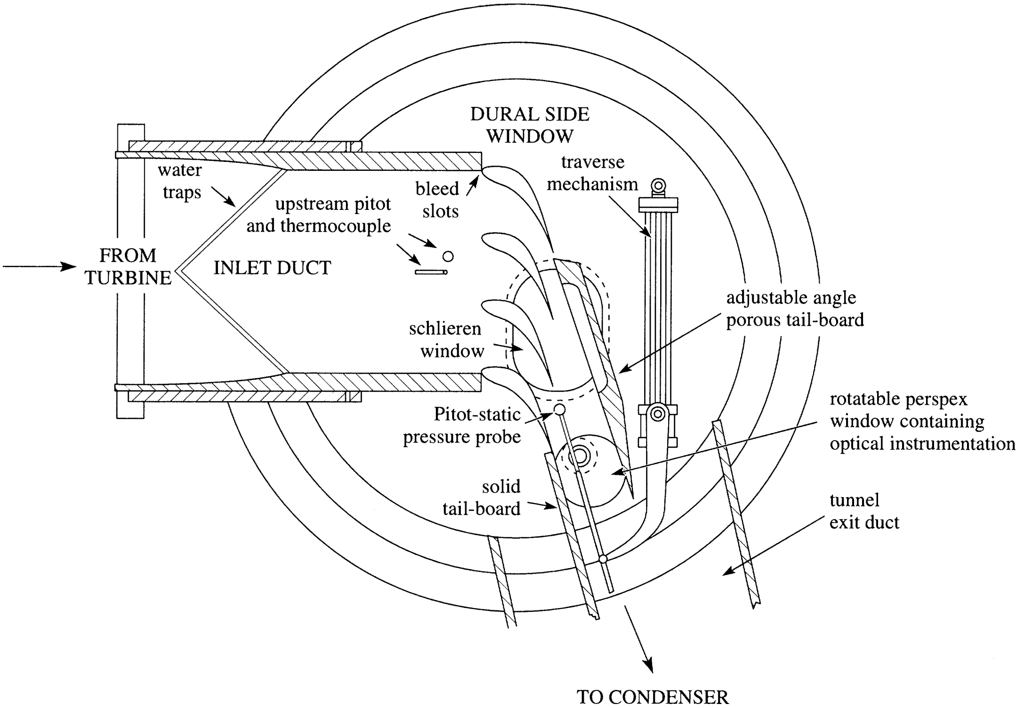

Figure 1. Details of the test section.

The droplets produced by homogeneous nucleation would then have been extremely small and difficult to measure. The use of large blades also facilitated the installation of comprehensive instrumentation and, in particular, enabled the inclusion of blade surface pressure tappings extending as far as the blade trailing edge, where condensation effects were most significant.

The mass flowrate available from the boilers limited the number of full-sized blades to four, thus providing three passages as shown in figure 1. This is the minimum number that could be used for an acceptable validation of a computer code incorporating periodic boundary conditions modelling an infinite cascade. Nevertheless, it was still necessary to reduce the inlet pressure from 0.5 bar (the design value) to 0.4 bar to obtain choking in the cascade.

The principal parameters governing compressible nucleating steam flow are listed in table 1. There is a close correspondence between the actual conditions within the turbine operating at design and those selected for the cascade experiments. The greatest discrepancy is for the Reynolds number where the difference is 25%. However, for Reynolds numbers of this magnitude, transition to turbulence in the boundary layers would probably occur over the first 30% of the blade, well upstream of the condensation zone in the experiments.

Since one of the objectives was to investigate the possibility of unsteady condensation occurring in the blade passages, it was important to eliminate spurious oscillations caused by the interaction of the trailing edge shock wave system and the free shear-layers generated by the blades at the upper and lower edges of the cascade. Such oscillations have been reported in the literature for cascade tests using air (Sieverding 1976) and are particularly likely to occur at exit Mach numbers close to unity. Furthermore, since the cascade contained only three passages, some

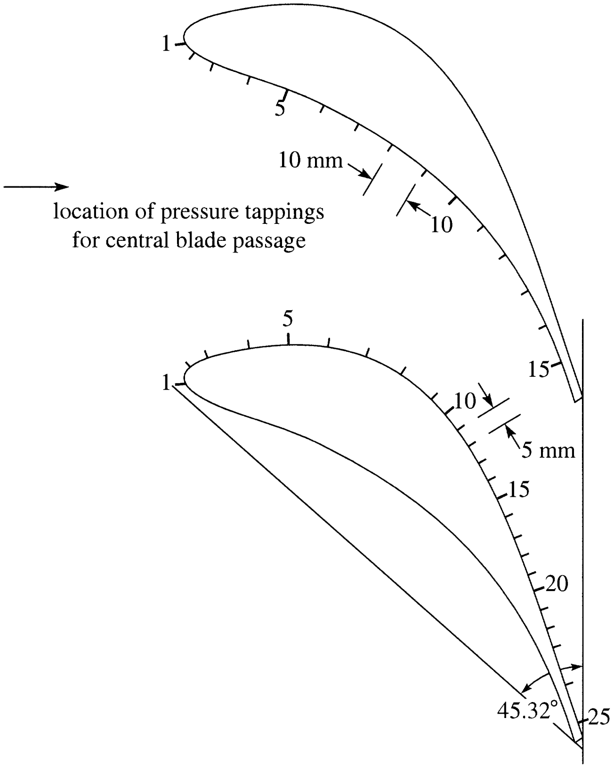

Figure 2. Fifth stage LP turbine stator blade geometry used for all the experiments: blade pitch 87.59 mm, blade chord 137.51 mm, stagger angle 45.32°, inlet flow angle 0.0°.

Table 1. *Principal dimensionless parameters governing the flow*

parameter	effects	cascade value	turbine value
mean expansion rate $\dot{P} = \dfrac{D(\ln P)}{Dt}$	Extent of departures from equilibrium	$-1156\ s^{-1}$	$-1156\ s^{-1}$
h_{fg}/c_pT_0	impact of heat addition for a given level of condensation	3.40	3.30
isentropic exit Mach number	downstream flow. Shock wave strength and orientation	1.03–1.35	1.20
Reynolds number $Re = \rho V c_x/\mu$	boundary layer growth and transition to turbulence	8.1×10^5	9.8×10^5

development work was required in order to obtain the closest approach possible to periodicity in the downstream flowfield.

For most of the experiments, the exit flow was constrained by two tailboards, as shown in figure 3. These effectively provided a variable geometry nozzle downstream of the cascade and, for choked flow, the cascade exit condition was independent of the condenser pressure. A mechanism was installed to allow adjustment of the upper

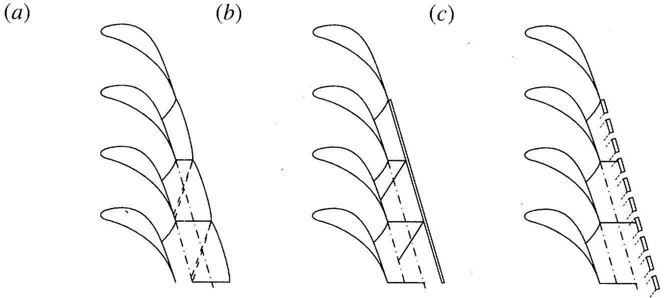

Figure 3. Different cascade downstream flow boundaries: (*a*) free shear-layer (constant pressure boundary); (*b*) solid tailboard (constant flow-angle boundary); (*c*) porous tailboard (mixed boundary).

tailboard angle (and hence exit Mach number) while tests were in progress. Several studies on the use of tailboards may be found in the literature (Gostelow 1984) and these conclude that tailboards with a perforated surface cause less disruption to the flow than either solid tailboards or free shear-layers. Ideally, the porosity of the tailboard should be adjustable to optimize cancellation of the shock waves at different conditions. Both solid and porous surfaces were tested and comparison between the results is discussed below.

Details of the final design of porous tailboard are illustrated in figure 4. The porosity was gradually phased in from the blade trailing edge, as shown, in order to prevent sudden expansion of the flow into the tailboard plenum. A system of ducts leading to the condenser was also installed, enabling variable suction to be applied to the tailboard plenum.

3. Instrumentation

(*a*) *Upstream measurements*

Since the incoming flow was taken from the very large plenum of the steam tunnel, the flow at inlet to the cascade was assumed to be uniform. Inlet conditions were obtained from single point measurements of total pressure and total temperature with a Pitot probe and hooded thermocouple, respectively. In the case of wet inflow, the wetness fraction was calculated approximately from the turbine work output, and the mean diameter of the incoming droplets was estimated from the known characteristics of the tunnel, established previously by a systematic program of optical measurements.

(*b*) *Blade surface pressure tappings*

Emphasis was placed on obtaining sufficient surface pressure data for code validation. Pressure tappings were therefore distributed over the entire pressure and suction surfaces of the central blade passage, as shown in figure 2. Pressure lines were lead out from the test section via hypodermic steel tubing contained within the blade bodies and measurements were made using a single digital transducer, connected to the tappings by a scanivalve arrangement. To prevent blockage of the pressure lines with condensate, the well-established practice of air purging was used. During measurement, however, all purge air flow was discontinued to avoid local distortion of the flow. Under these conditions, the pressure indicated by the transducer fell to the level at the blade surface in a few seconds.

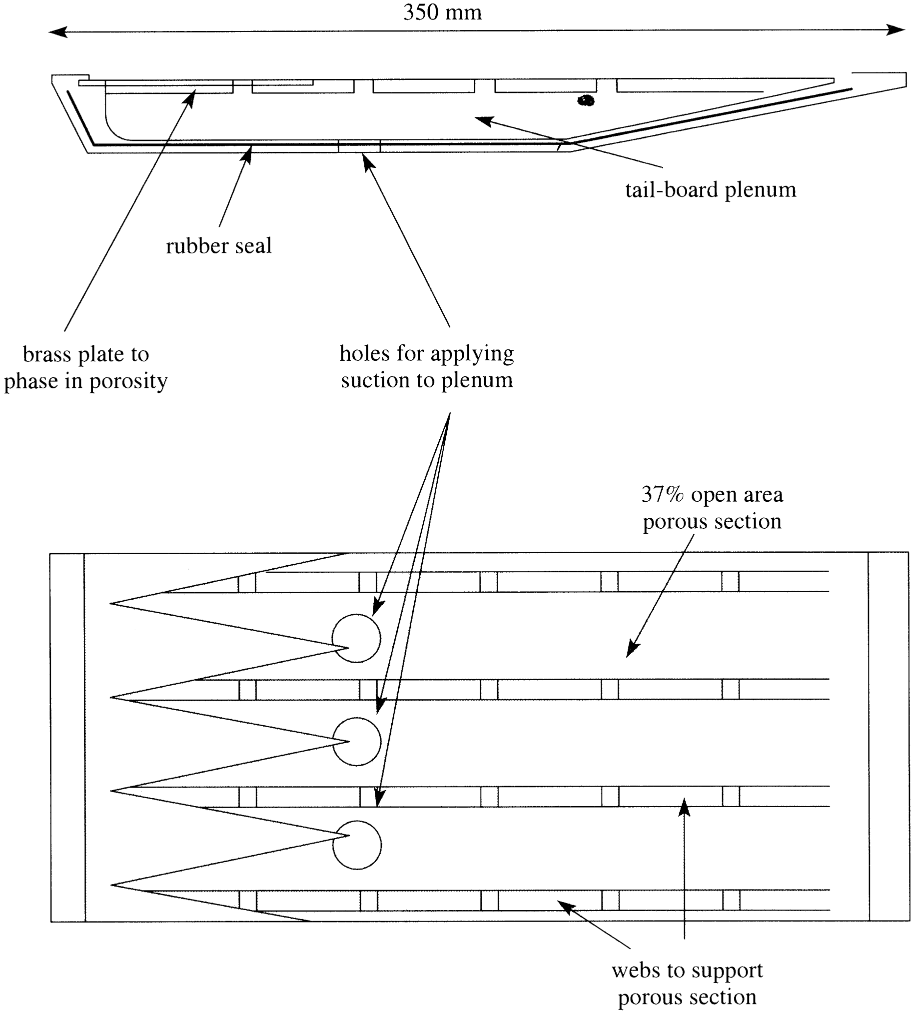

Figure 4. Details of the porous tailboard.

(*c*) *Outlet plane traverses*

For the purpose of establishing exit Mach numbers and blade losses, total and static pressure measurements were made one quarter of an axial chord length downstream of the blade trailing edges. The traverse mechanism and probe attachment can be seen in figure 1.

The measurements were made with the combined total and static probe shown in figure 5. Prior to installation, the static pressure probe was calibrated in steam in a special porous calibration section. The effect of inclining the probes to the flow direction was also investigated and found to be negligible up to incidences of ±10° for both total and static pressure measurements. The effects of vapour-droplet thermal and inertial relaxation on the response of the total pressure probe are of paramount importance when interpreting the raw measurements and these aspects are discussed later in the paper.

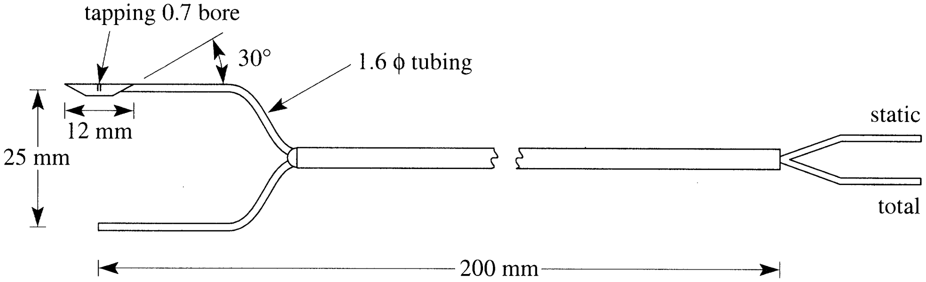

Figure 5. Total and static pressure probes used for traversing downstream of the cascade.

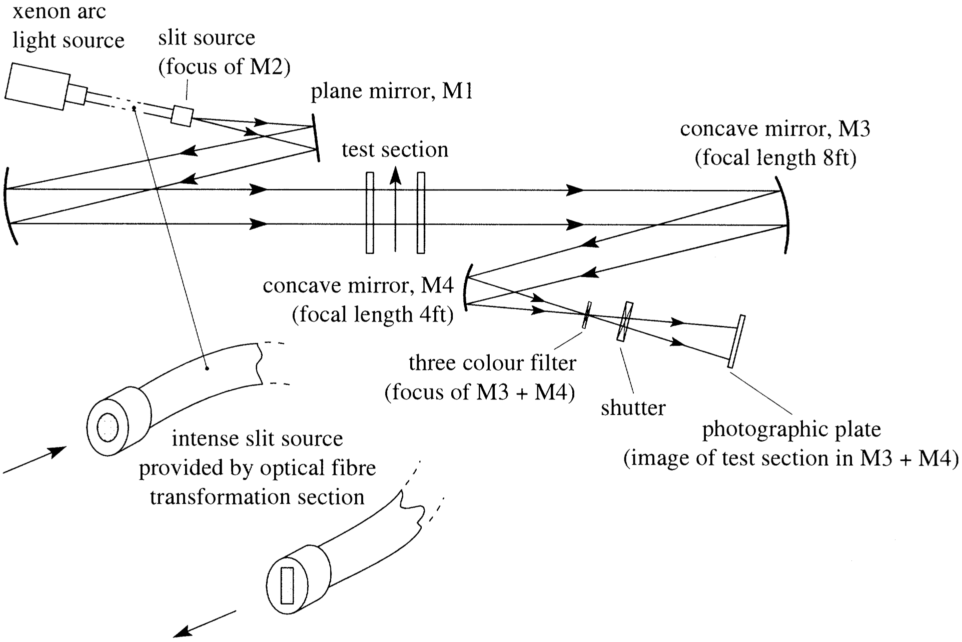

Figure 6. Schematic view of the schlieren arrangement.

(*d*) *Schlieren flow visualization*

The schlieren arrangement is shown schematically in figure 6. As a result of the long focal length of the schlieren optics, it was necessary to ‘wrap’ the optical path. However, angles were kept to a minimum in order to minimize aberration.

Colour visualization proved particularly useful since, with correct alignment of the three-colour filter, shock and expansion waves could be distinguished as bands of blue and red, respectively. Illumination was provided by a xenon arc lamp combined with a fibre-optic transformation section, as shown in figure 6. This proved a particularly effective way of providing an intense slit source. The use of a fine coating of ‘milk of magnesia’, in addition to the sidewall water traps, successfully prevented contamination of the windows with condensate.

(*e*) *Optical droplet sizing*

Droplet sizes were obtained from measurements of light extinction over a range of wavelengths using the optical system described by Skillings (1989). The accuracy of the measurements for monodispersed droplets was originally established using laboratory generated hydrosols, as described by Walters (1973). Later developments allowed entire droplet size distributions to be successfully computed from measurements in turbines (Walters 1985), but, for the present cascade experiment, it was only possible to obtain an average droplet size. This was because the variation of light extinction with wavelength showed very little curvature for the range of droplet sizes produced in the cascade and, consequently, the processing required to obtain the complete dispersion became very 'ill-conditioned'. In order to examine the influence of cross-passage variations in expansion rate, the perspex windows containing the optics could be rotated, thus allowing a downstream 'traverse' consisting of three separate optical measurements across one blade passage (see figure 1).

4. Theoretical calulation procedure

Numerical predictions for comparison with the experimental measurements were generated by a computer program which simulated condensing steam flow in two-dimensional turbine cascades. Viscous effects were not included but the numerical procedure was time-accurate and could model periodically unsteady condensation processes. An outline of the theory is provided below and full details can be found in White & Young (1993).

Wet-steam is assumed to be a mixture of vapour at pressure P, temperature T_g and density ρ_g, and a large number of spherical liquid droplets of various sizes. The continuous distribution of droplet sizes is discretized into a finite number of droplet groups, the ith group containing n_i droplets per unit mass of mixture, each of radius r_i, temperature T_i and density ρ_f (the liquid being assumed incompressible). The wetness fraction y is then given by

$$y = \sum_i y_i = \sum_i \tfrac{4}{3}\pi r_i^3 \rho_f n_i, \tag{4.1}$$

and the mixture density ρ by

$$\frac{1}{\rho} = \frac{1-y}{\rho_g} + \sum_i \frac{y_i}{\rho_f} \approx \frac{1-y}{\rho_g}, \tag{4.2}$$

The mixture specific internal energy e, enthalpy h and entropy s can be expressed as

$$e = (1-y)e_g + \sum_i y_i e_i, \tag{4.3}$$

$$h = (1-y)h_g + \sum_i y_i h_i, \tag{4.4}$$

$$s = (1-y)s_g + \sum_i y_i s_i, \tag{4.5}$$

where the liquid terms include contributions from the surface energy and entropy. The vapour phase properties are calculated from the equation of state described by Young (1992).

In general, the two phases are not in equilibrium, so the temperatures T_g and T_i differ from the saturation temperature $T_{\mathrm{s}} = T_{\mathrm{s}}(P)$. A convenient measure of departures from thermal equilibrium is the 'vapour subcooling' $(T_{\mathrm{s}} - T_g)$, this being closely related to the deviation of the wetness fraction from its local equilibrium value (Young 1984). The droplet temperatures are given by Gyarmathy's approximation:

$$T_i = T_\mathrm{s} - \frac{2\sigma_i T_\mathrm{s}}{\rho_f h_{fg} r_i}, \tag{4.6}$$

σ_i being the surface tension of group-i droplets. In contrast to the vapour, the droplet temperatures relax extremely rapidly to their equilibrium value and, except for very tiny droplets in the early stages of nucleation, $T_i \approx T_\mathrm{s}$.

Neglecting interphase velocity slip (a good approximation for self-nucleated droplets), the conservation equations of mass, momentum and energy for the inviscid adiabatic compressible flow of the mixture are identical to their single-phase counterparts:

$$\frac{\partial \rho}{\partial t} + \nabla \cdot (\rho \boldsymbol{u}) = 0, \tag{4.7}$$

$$\frac{\partial \boldsymbol{u}}{\partial t} + (\boldsymbol{u} \cdot \nabla)\boldsymbol{u} + \frac{\nabla P}{\rho} = 0, \tag{4.8}$$

$$\frac{\partial (\rho E)}{\partial t} + \nabla \cdot (H \rho \boldsymbol{u}) = 0, \tag{4.9}$$

where $\boldsymbol{u}$ is the common velocity of the phases, $E = e + \frac{1}{2}u^2$ and $H = h + \frac{1}{2}u^2$.

Mathematical closure of these equations requires a separate equation for the wetness fraction and this is obtained from the theories of nucleation and droplet growth. The rate of formation of droplet embryos per unit mass of mixture J is obtained from the classical theory of non-isothermal homogeneous nucleation:

$$J = \frac{q_\mathrm{c}}{1+\phi} \left(\frac{2\sigma_g}{\pi m^3} \right)^{1/2} \frac{\rho_g}{\rho_f} \exp\left(-\frac{4\pi r_*^2 \sigma_g}{3kT_g} \right), \tag{4.10}$$

where k is Boltzmann's constant, q_c is the condensation coefficient (assumed to be unity), m is the mass of a molecule, r_* is the Kelvin–Helmholtz critical radius and $(1+\phi)$ is the non-isothermal correction factor. The definition of r_* and ϕ are standard and can be found, with discussion, in Young (1982, 1992). The precise form of the nucleation equation is still controversial but calculations based on equation (4.10) give good agreement with one-dimensional condensing nozzle experiments.

The equation representing the growth rate of group-i droplets is a slightly modified version of the standard Gyarmathy equation:

$$(h_g - h_i)\frac{\mathrm{D}r_i}{\mathrm{D}t} = \frac{\lambda_g (T_i - T_g)}{\rho_f r_i [1 + 1.89(1-\nu) l_g / \mathit{Pr}_g]}, \tag{4.11}$$

where λ_g and Pr_g are the thermal conductivity and Prandtl number of the vapour, respectively, l_g is the mean free path of a vapour molecule and $\mathrm{D}/\mathrm{D}t$ is the substantive derivative. The factor $(1-\nu)$ is a semiempirical correction factor which is included to obtain precise agreement with droplet size measurements in LP nozzle experiments. The physical reason as to why the agreement between theory and experiment deteriorates slightly at very low Wilson point pressures has never been satisfactorily explained. However, pending improvements to the theories of nucleation and droplet growth, inclusion of the small correction $(1-\nu)$ does successfully side-step the difficulty (and can be justified on physical grounds if the condensation and evaporation coefficients were to differ under non-equilibrium conditions). The original prescription of Young (1982) for the factor $(1-\nu)$ was modified slightly by White & Young (1993) and it is the latter form which has been adopted here. ($\nu \approx 0.2$ for the calculations described below.)

The rate of change of wetness fraction along a pathline (in unsteady flow) or a streamline (in steady flow) is thus given by

$$\frac{\mathrm{D}y}{\mathrm{D}t} = \sum_i \frac{\mathrm{D}y_i}{\mathrm{D}t} \approx \sum_i 4\pi r_i^2 \rho_f n_i \frac{\mathrm{D}r_i}{\mathrm{D}t} = \sum_i \frac{3y_i}{r_i} \frac{\mathrm{D}r_i}{\mathrm{D}t}, \tag{4.12}$$

where the $\mathrm{D}r_i/\mathrm{D}t$ are given by equation (4.11) and the n_i are obtained by integrating the nucleation rate J along the relevant pathline or streamline.

The H-mesh computational grid used for the numerical solution of the equations is shown in figure 7. The conservation equations (4.7–4.9) are written in finite volume form and are marched forward in time using a second-order time-accurate Runge–Kutta algorithm similar to that developed for perfect gas applications by Jameson *et al.* (1981). Details of the discretization, the artificial viscosity, the boundary conditions and other aspects of the technique can be found in White & Young (1993).

Since the time derivatives of equations (4.11) and (4.12) are all substantive, the droplet radii and wetness fraction are most conveniently obtained by integrating along fluid pathlines. For this purpose, at each time-step, the velocity field obtained by the Runge–Kutta solution of equations (4.7–4.9) is used to determine the instantaneous trajectories of fluid particles, as illustrated in the diagram of figure 7. The integration of equation (4.12) is then performed along the pathline using a predictor–corrector method, the results being transferred to the solution procedure for the conservation equations in readiness for the next time increment. A major advantage of this mixed Eulerian–Lagrangian approach is that the integration of equation (4.12) involves thermodynamic states only and hence this part of the coding is completely decoupled from the fluid dynamic section once the pathline has been identified (Young 1992).

5. Test conditions

Details of the experimental conditions for all the cascade tests are given in table 2. For all the tests, the inlet stagnation pressure was maintained at about 0.4 bar. Four different levels of inlet superheat ΔT_0 were then investigated. These are classified in table 2 as L (low, $\Delta T_0 = 4$–$8\,^\circ\mathrm{C}$), M (medium, $\Delta T_0 = 13$–$15\,^\circ\mathrm{C}$), H (high, $\Delta T_0 = 26$–$28\,^\circ\mathrm{C}$) and F (very high, $\Delta T_0 = 39\,^\circ\mathrm{C}$). Some tests with an inlet wetness of about 1.6%, classified W, were also made. For each category of inlet condition (L, M, H, F, W), tests were carried out at three different tailboard angles, giving exit isentropic Mach numbers M_{2s} in the range 1.05–1.35. A few tests, classified D, were also conducted to compare the performance of solid and porous tailboards, and to investigate the flow without tailboards.

6. Experimental results and comparison with theory

In this discussion, the Mach numbers referred to are the average isentropic exit values M_{2s} based on the total-to-static pressure ratio P_{01}/P_2 and an isentropic exponent of $\gamma = 1.32$. ΔT_0 denotes the inlet stagnation superheat, $T_{01} - T_\mathrm{s}(P_{01})$. Due to space limitations, it is only possible to present a selection of results but further details can be found in White (1992).

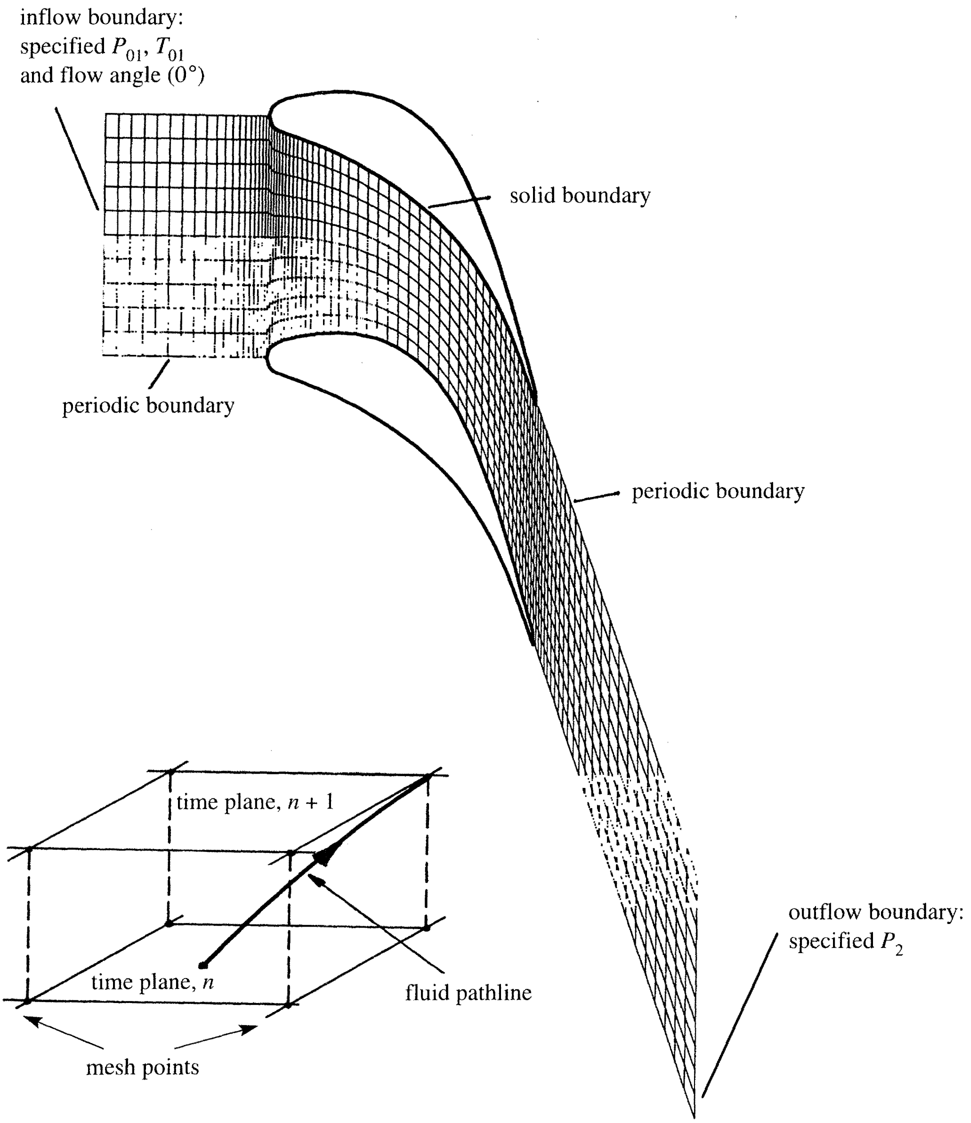

Figure 7. Details of the computational H-mesh and the fluid pathline used for integration of the droplet growth equations for unsteady flow predictions.

(*a*) *Schlieren flow visualization*

(i) *Unconstrained exit flow*

Higher exit Mach numbers could be achieved when the flow was unconstrained by tailboards and it is useful to describe this situation first in order to identify the various flow features. Figure 8 shows the schlieren photograph and predicted pressure contours for test D1. The blue shock wave pattern consists of the usual trailing edge shock waves observed in single-phase flow, S_p and S_s, and an additional feature S_c. The branching of S_p and S_s is due to the flow being beyond 'limit load' (i.e with an axial Mach number greater than unity). Rapid expansions near the trailing edge can be seen as regions of red.

Table 2. *Test conditions*

	upstream conditions			downstream conditions		
test number	stagnation pressure P_{01} (mbar)	stagnation temperature T_{01} (K)	stagnation superheat $T_{01} - T_s(P_{01})$ (deg)	tailboard angle (°)	mean static pressure P_2 (mbar)	isentropic Mach No. M_{2s}
L1	403	354.0	4.5	67.5	163	1.24
L2	409	354.0	4.0	68.9	194	1.11
L3	417	357.5	7.5	70.2	206	1.08
M1	416	364.0	15.0	67.5	169	1.24
M2	417	364.5	14.5	68.9	191	1.14
M3	427	364.0	13.5	70.2	212	1.08
H1	437	378.0	27.0	67.5	152	1.35
H2	419	378.5	28.0	68.9	177	1.20
H3	414	376.0	26.0	70.2	194	1.10
F1	435	390.0	39.0	68.0	163	1.30
F2	435	390.0	39.0	69.2	176	1.24
F3	435	390.0	39.0	70.8	197	1.15
W1	419	350.0	wet ($\sim$ 1.6%)	67.5	178	1.20
W2	419	350.0	wet ($\sim$ 1.6%)	68.9	200	1.11
W3	414	350.0	wet ($\sim$ 1.6%)	70.2	213	1.05
D1	410	352.5	3.0	none	$\sim$ 115	$\sim$ 1.50

Reducing the exit Mach number by raising the condenser pressure caused S_p and S_s to become more normal to the flow direction, just as in single-phase flow (Lichtfuss & Starken 1976), while the location of S_c did not change. In contrast, increasing the inlet superheat caused S_c to move downstream while the positions of S_p and S_s remained fixed. This clearly suggests that S_c is caused by condensation heat release: increasing the inlet superheat delays phase transition, thus causing a downstream migration.

As with single-phase calculations, the time-marching scheme has difficulty in predicting S_p, which appears in the pressure contours only as a slight pressure rise extending part-way across the passage. However, the calculated Wilson points correspond very closely to S_c, providing further evidence that this feature is due to condensation. (Note that S_c is sharply defined in the photograph implying that it includes a real flow discontinuity.)

The untailboarded tests were also used to ensure that constraining the exit flow did not inhibit unsteadiness due to supercritical condensation heat release. A brief exploration of all possible combinations of inlet and outlet conditions revealed general unsteadiness typified by the blurring of shock waves, such as S_p and S_s in figure 8. It was concluded that this was due to the interaction between the suction

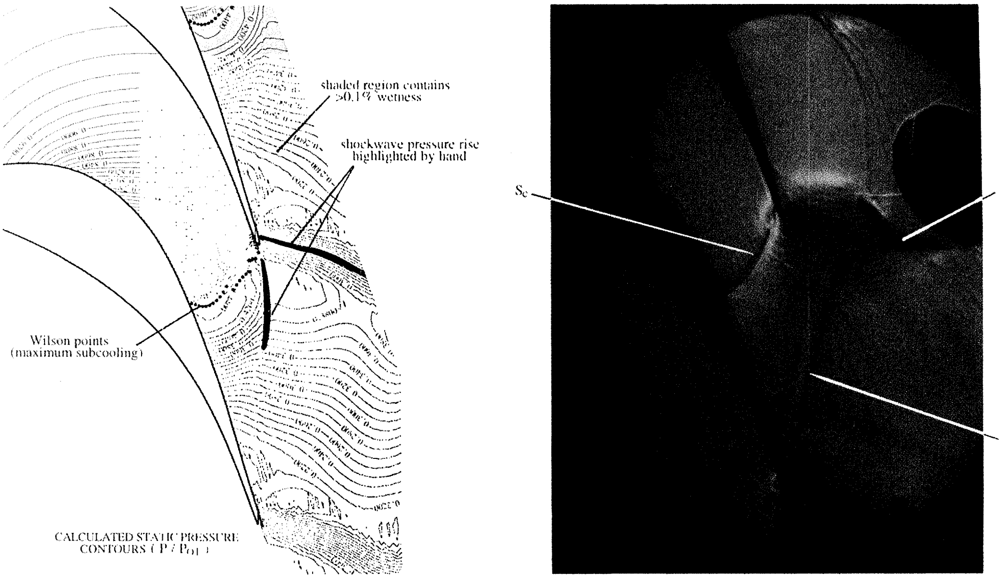

Figure 8. Test D1: dry inflow, $\Delta T_0 = 3.0\,^{\circ}\mathrm{C}$, $M_{2s} = 1.5$, unconstrained exit flow.

surface shock wave emanating from the uppermost blade and the free shear-layer. Downstream Pitot traverses also showed that the cascade exit flow was highly unperiodic. Evidently, the untailboarded cascade did not provide a suitably controlled environment for investigating either steady or unsteady flows.

(ii) *Comparison of solid and porous tailboards*

The effects of solid and porous tailboards were examined by performing tests with sufficiently high inlet superheat that the flow remained dry throughout the cascade. In both cases, the flow was much steadier than in the untailboarded situation and the shock waves S_p and S_s were very sharply defined in the schlieren photographs. As expected, the solid tailboard caused a reflection of the shock wave S_s which impinged on the suction surface of the central blade near the trailing edge, resulting in a spurious pressure rise which would have severely hampered validation of the theoretical calculations. The porous tailboard, on the other hand, although successfully cancelling S_s, resulted in a weak reflected expansion wave. Applying suction to the tailboard plenum did not affect this situation, probably because the degree of suction was insufficient. However, the flow with the porous tailboard was more periodic and hence all subsequent tests were conducted with this configuration.

(iii) *High inlet superheat*

Figure 9 shows the schlieren photograph and computed pressure contours for test H2 ($\Delta T_0 = 28.0\,^{\circ}\mathrm{C}$, $M_{2s} = 1.20$). Mach numbers in excess of 1.5 were predicted on the suction surface and in such regions the subcooling is sufficient to cause spontaneous nucleation, despite the high inlet superheat. Immediate phase transition is suppressed, however, by the temperature rise through S_s and significant moisture does not appear until further downstream. This accounts for the absence of the feature S_c, for the impact of the condensation heat release on the gas dynamics, when it does occur downstream at comparatively high Mach number, is much less pronounced than in figure 8. The schlieren photograph in figure 9 also shows a suction

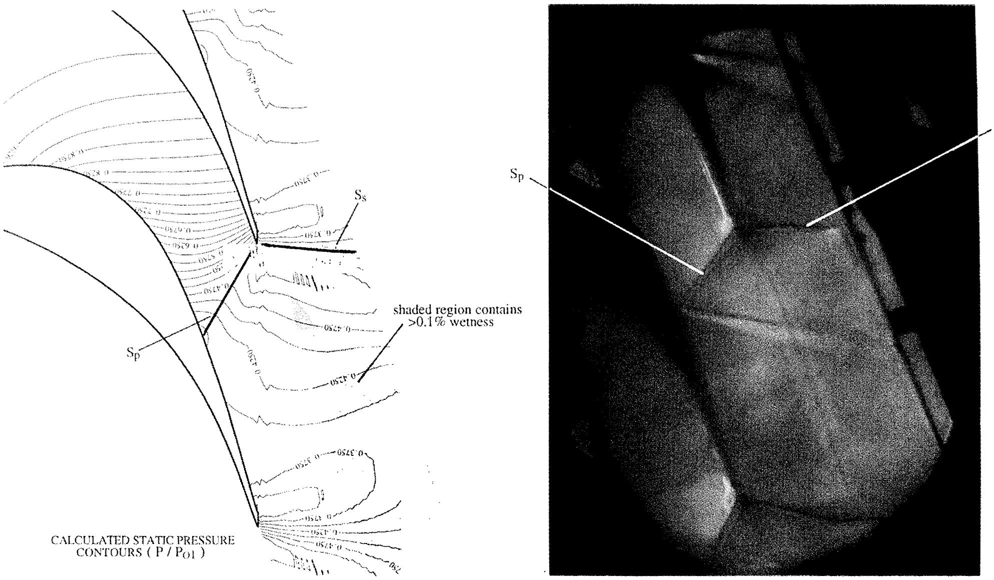

Figure 9. Test H2: dry inflow, $\Delta T_0 = 28.0\,^{\circ}\mathrm{C}$, $M_{2s} = 1.20$, porous tailboard.

surface reflection of S_p which is not reproduced by the calculations. This is due to the skewness of the computational grid downstream of the blade and is a well known problem associated with H-meshes of the type used.

Regions of wetness greater than 0.1% have been shaded on the contour plot and show that, due to the cross-passage variation, moisture is most pronounced in the flow convected from near the suction surface. The approximate boundary between wet and dry flow was also determined experimentally using a hand-held laser. By directing the laser beam into the flow, the regions of condensation became visible from the light scattered by the droplets. These observations confirmed the predictions of the theory.

(iv) *Low inlet superheat*

The schlieren photographs and predicted pressure contours for the three low superheat tests L1, L2 and L3 are shown in figures 10–12. These are particularly interesting because the pressure surface shock wave S_p and the condensation zone interact as the exit Mach number is reduced.

For test L1, figure 10 ($\Delta T_0 = 4.5\,^{\circ}\mathrm{C}$, $M_{2s} = 1.24$), the shock wave pattern is quite different from that for Test H2, figure 9 ($\Delta T_0 = 28.0\,^{\circ}\mathrm{C}$, $M_{2s} = 1.20$). First, the main feature propagating across the central blade passage is curved and does not reflect from the suction surface. Second, two distinct shock waves can be distinguished emanating from the pressure surface: the usual shock wave S_p and the feature S_c associated with condensation. S_p extends only part-way across the passage before merging with S_c. The calculations show a clear pressure rise spanning the entire blade passage and coinciding with S_c in the photograph. (A separate feature corresponding to S_p is not discernible.) The predicted onset of condensation, as shown by the shaded region, and the locus of maximum subcooling also agree well with the position of S_c.

Test L2, figure 11 ($\Delta T_0 = 4.0\,^{\circ}\mathrm{C}$, $M_{2s} = 1.11$) corresponds to a reduction in exit Mach number and this causes S_p to rotate upstream and pass through the condensation zone. As shown by the calculations, this results in part of the condensation

PHILOSOPHICAL TRANSACTIONS OF THE ROYAL SOCIETY A MATHEMATICAL, PHYSICAL & ENGINEERING SCIENCES

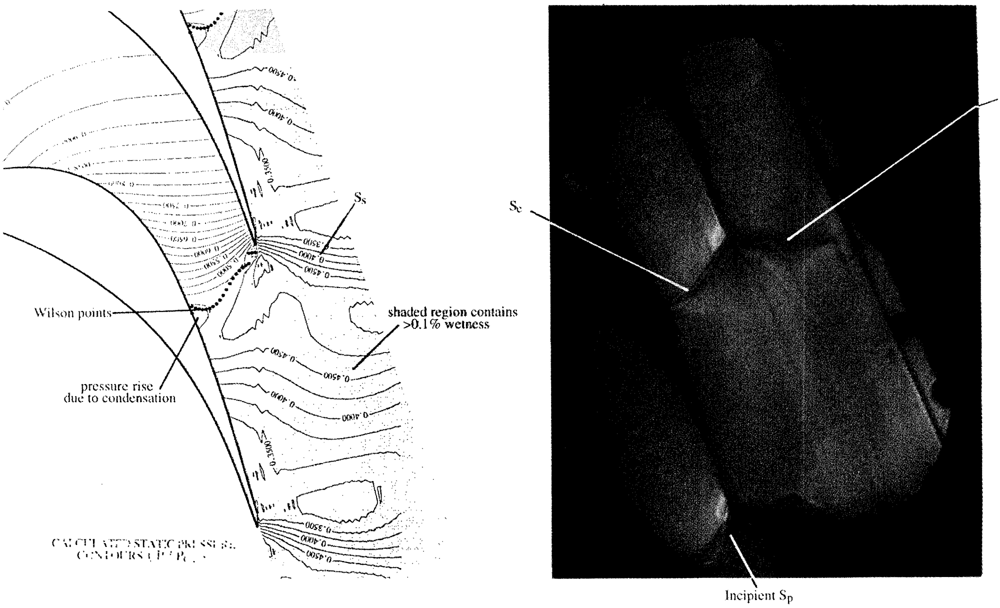

Figure 10. Test L1: dry inflow, $\Delta T_0 = 4.5\,^{\circ}\mathrm{C}$, $M_{2s} = 1.24$, porous tailboard.

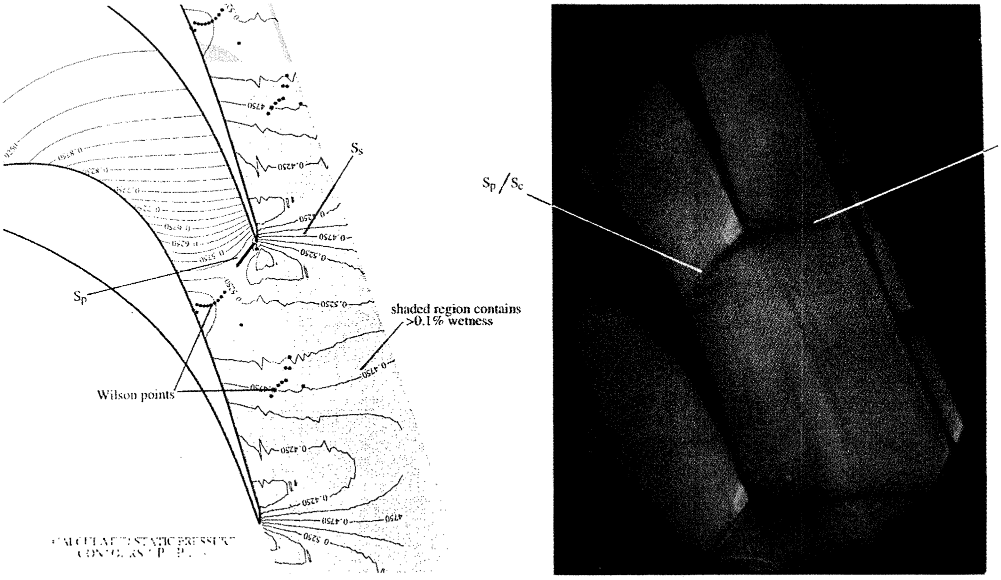

Figure 11. Test L2: dry inflow, $\Delta T_0 = 4.0\,^{\circ}\mathrm{C}$, $M_{2s} = 1.11$, porous tailboard.

front being displaced downstream (due to the temperature rise through S_p) while the part near the suction surface retains its original position. The schlieren photograph shows the shock wave S_p and the condensation front S_c corresponding closely to the theoretical predictions. The shock wave pattern in this situation is very sensitive to small disturbances and careful study reveals that S_c and S_p are quite blurred, suggesting that they may have been oscillating slightly.

For test L3, figure 12 ($\Delta T_0 = 7.5\,^{\circ}\mathrm{C}$, $M_{2s} = 1.08$), the exit Mach number has been

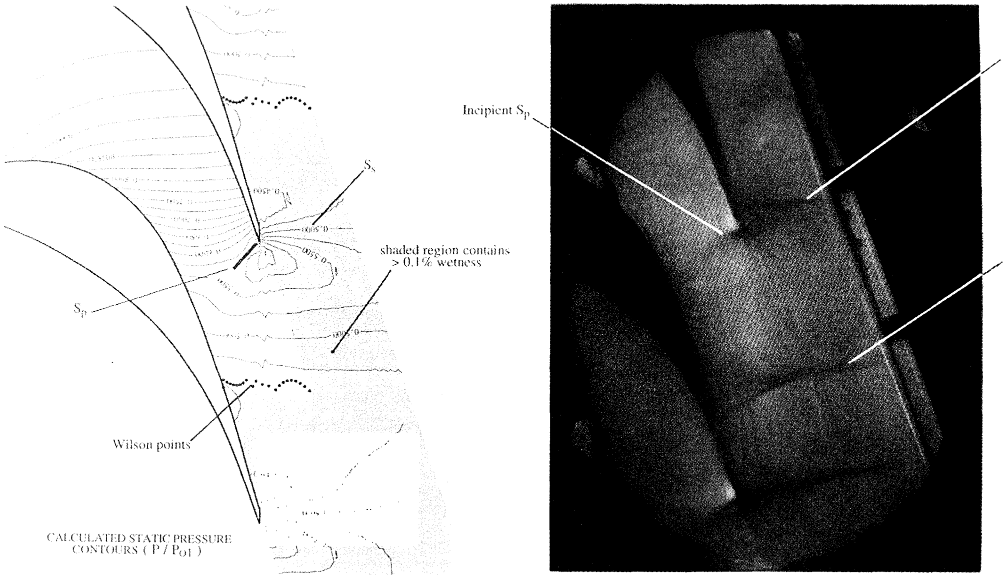

Figure 12. Test L3: dry inflow, $\Delta T_0 = 7.5\,^\circ\mathrm{C}$, $M_{2s} = 1.08$, porous tailboard.

reduced even further and the entire condensation front is displaced downstream. In the photograph, the onset of condensation is clearly visible at approximately the same location as the predicted locus of the Wilson points. (This feature was absent for the high superheat cases.) The sensitivity of the flow structure is emphasized by the fact that the exit Mach number is only 0.03 lower than for test L2, yet the shock wave pattern is completely different.

(v) *Wet inflow*

Based on the power output from the turbine, the inlet wetness was estimated to be 1.6%. Downstream light extinction measurements for test W3 indicated a strongly bimodal droplet size distribution, providing evidence that secondary nucleation occurred in the cascade. The mean radius of the larger droplet mode was known to be about 0.5 µm although, for the calculations, the inlet droplet radius was set to 0.6 µm, since at smaller radii no appreciable secondary nucleation was predicted.

The shock wave patterns of the schlieren photographs show similar variations as the low inlet superheat tests (L1, L2 and L3, figures 10–12). This is because condensation onto the droplets already present in the flow releases heat to the vapour, thus delaying the onset of the secondary nucleation. In this respect, the effect of the primary droplets is similar to that of raising the inlet temperature slightly above the saturation value: homogeneous nucleation occurs further downstream than if the flow had been dry saturated.

For test W1, figure 13 ($y_0 \approx 1.6\%$, $r_0 \approx 0.6$ µm, $M_{2s} = 1.20$), the curvature of S_c and the double shock wave $S_\mathrm{c}/S_\mathrm{p}$ suggest the presence of rapid secondary condensation. This is confirmed by the predictions, as shown by the shaded area which indicates regions containing more than one droplet size group. No corresponding feature is seen on the static pressure contours, probably because large departures from equilibrium are prevented by condensation onto the primary droplets.

For tests W2 and W3, the secondary nucleation was displaced downstream. Agreement with the theoretical predictions was not as good as for the other tests but this

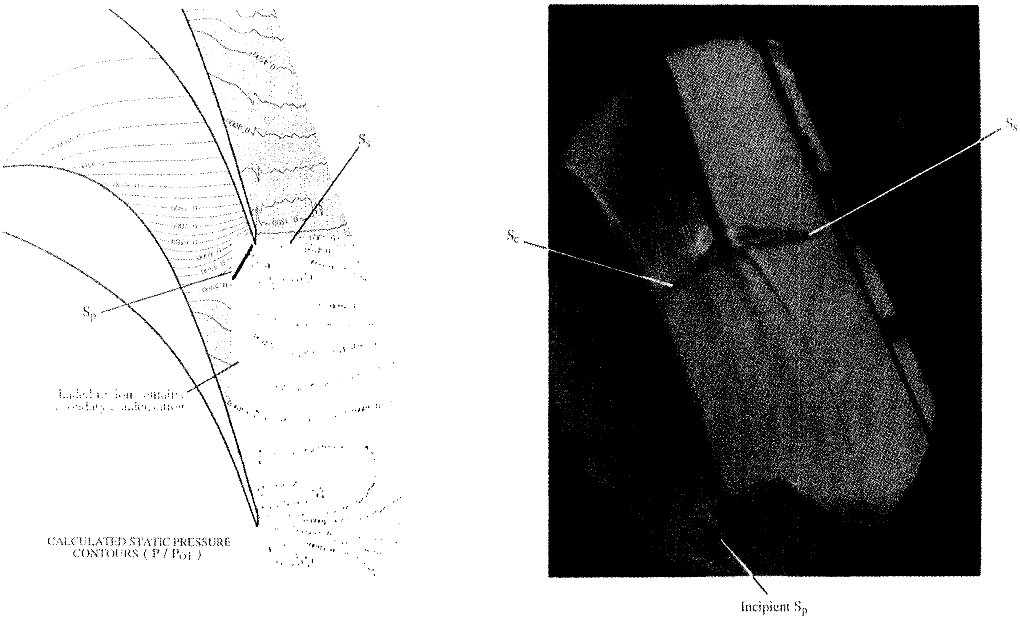

Figure 13. Test W1: wet inflow, $y_0 \approx 1.6\%$, $r_0 \approx 0.6$ μm, $M_{2s} = 1.20$, porous tailboard.

was almost certainly the result of small errors in the estimated inlet wetness fraction and droplet size. Indeed, the predictions and the experiments could easily be brought into close correspondence by making quite small adjustments to the inlet parameters.

(*b*) *Blade surface static pressure distributions*

Comparisons between the calculated and measured surface pressure distributions are shown in figure 14. In all cases, agreement is good for the entire pressure surface and for the suction surface up to the sonic point. It is only downstream of this point that there are significant discrepancies, but this, of course, is also the region in which the effects of condensation are most apparent. The main computational difficulty is that the trailing edge shock wave system cannot be accurately resolved by the inviscid Euler solver. Nevertheless, not all discrepancies should be attributed to deficiencies in the numerical scheme. With only three passages in the cascade, it is impossible to obtain a perfectly periodic cascade exit flow and, despite the considerable efforts made, it is likely that disturbances reflected from the upper tailboard did affect the suction surface distributions.

(i) *High inlet superheat*

When the inlet superheat is greater than about 25 °C (tests F and H), the effects of condensation are not apparent on the surface pressure distributions (except for the high exit Mach number test H1, where spontaneous nucleation occurs on the suction surface). Dry perfect gas calculations thus yield almost identical results to the full wet-steam calculations. The main feature of the suction surface measurements is the impingement of the shock wave S_p, which migrates upstream with decreasing exit Mach number. A typical example is shown in figure 14*a* for tests H3 ($\Delta T_0 = 26.0\,^\circ\mathrm{C}$, $M_{2s} = 1.10$) and F3 ($\Delta T_0 = 39.0\,^\circ\mathrm{C}$, $M_{2s} = 1.15$), having almost the same exit Mach numbers but different inlet superheats. Although the calculations smear the shock wave, its location is predicted correctly and this is true for all the other

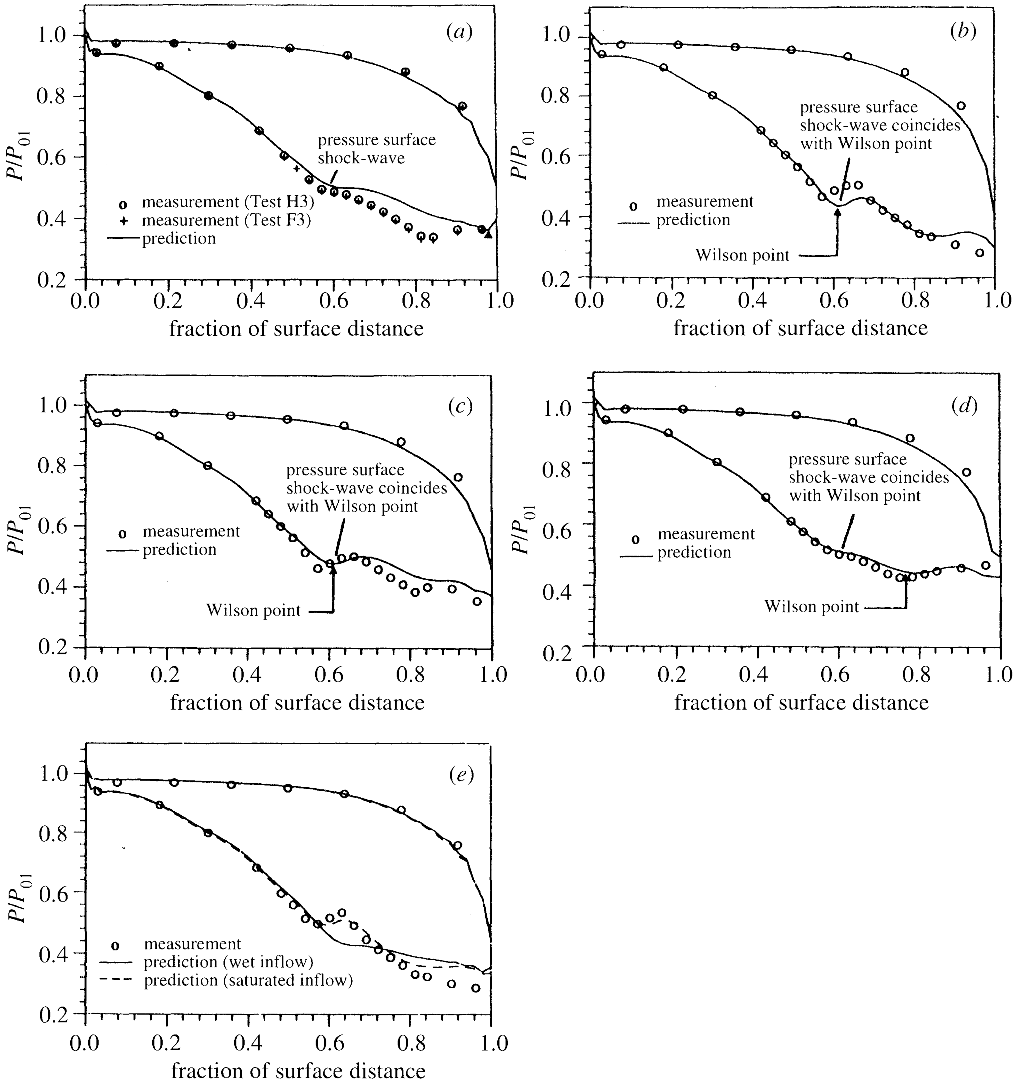

Figure 14. Blade surface pressure distributions: (*a*) tests H3 ($\Delta T_0 = 26\,^{\circ}\mathrm{C}$, $M_{2s} = 1.10$) and F3 ($\Delta T_0 = 39\,^{\circ}\mathrm{C}$, $M_{2s} = 1.15$); (*b*) test L1 ($\Delta T_0 = 4.5\,^{\circ}\mathrm{C}$, $M_{2s} = 1.24$); (*c*) test L2 ($\Delta T_0 = 4.0\,^{\circ}\mathrm{C}$, $M_{2s} = 1.11$); (*d*) test L3 ($\Delta T_0 = 7.5\,^{\circ}\mathrm{C}$, $M_{2s} = 1.08$); (*e*) test W1 ($y_0 = 1.6\%$, $r_0 = 0.6\,\mu\mathrm{m}$, $M_{2s} = 1.20$).

tests in categories H and F. Referring again to figure 8*a*, the measurements show a second pressure rise close to the trailing edge which is not seen in the predictions. This appeared in both tests H3 and F3 and cannot therefore be associated with condensation. It is most probably caused by reflections from the upper tailboard.

(ii) *Low inlet superheat*

Ironically, the predictions for these more complicated condensing flow cases (tests L1, L2 and L3) are in much closer agreement with the experimental measurements as shown by figures 14*b*–*d*. This is because the dominant feature appearing on the suction surface is now the pressure rise due to condensation and, unlike the dis-

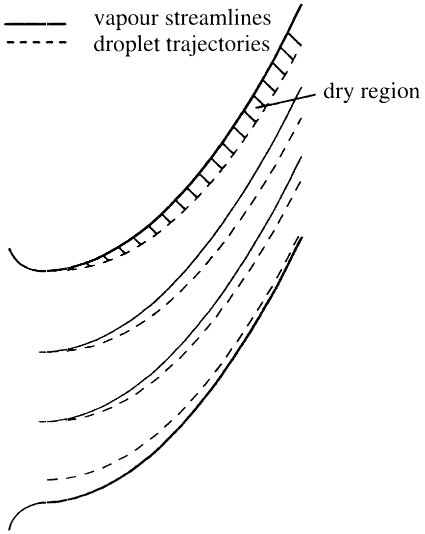

Figure 15. The effect of interphase velocity slip. Calculation by the method of Gyarmathy. The figure makes use of the following assumptions: (1) constant u_x along streamlines; (2) constant droplet radius (1.0 µm); (3) parabolic vapour streamline; and (4) no slip in x-direction.

continuous shock waves, this is accurately resolved by the calculations. The figures confirm the deductions from the schlieren photographs (figures 10–12): at the high and medium exit Mach numbers (tests L1 and L2), the shock wave S_{p} and the condensation front are coincident, whereas at the lowest exit Mach number (test L3), the condensation occurs downstream of S_{p}.

(iii) *Wet inflow*

A comparison between the calculated and measured pressure distributions for test W1 ($y_0 \approx 1.6\%$, $r_0 \approx 0.6$ mm, $M_{2s} = 1.12$) is shown in figure 8*e*, (see also figure 13). It is interesting to observe that, although a secondary nucleation was predicted in the supersonic region (the subcooling rising to more than 35 °C), the calculations did not indicate the usual rise in pressure. This was because condensation on the primary droplet group was sufficient to prevent excessive departures from equilibrium. The secondary nucleation was therefore less intense and persisted for a longer period. Also shown in figure 14*e* is the prediction for a dry saturated inflow condition. This is in much closer agreement with the measurements, implying that the primary droplet group in the experiments was almost inert to interphase transfer. In turn, this suggests that the experimental values of inlet wetness fraction and droplet size may have differed slightly from the assumed values as discussed in connection with the schlieren photographs.

An alternative explanation which may account for the discrepancies between calculations and measurements for the wet inflow tests is that inertial effects are likely to be significant for the large primary droplets. (It should be recalled that interphase velocity slip has been neglected throughout in the calculations.) The main effect of velocity slip is that it causes departures of the droplet trajectories from the vapour streamlines. Figure 15 shows trajectories for 1.0 µm droplets calculated by an approximate method due to Gyarmathy (1964). It is evident that the interphase slip leaves a region of dry flow close to the suction surface. Presumably, the steam here becomes subcooled and reverts to equilibrium via a homogeneous nucleation at about the same location as if its inlet condition were dry saturated.

(c) *Droplet size measurements*

Extracting the droplet size from the optical measurements involves matching measured light transmittances, defined as $T_\lambda = \ln\{(I/I_0)_\lambda\}$ (where I and I_0 are the transmitted and incident light intensities for wavelength λ), with values given by the Mie theory. T_λ may be shown to be a function of the particle size parameter $\alpha = 2\pi r/\lambda$. Thus, if measured values of T_λ are plotted against $1/\lambda$ on a log–log scale and matched with the theoretical values plotted against α on the same basis, the droplet size is given by the relative displacement of the abscissae (Walters 1973, 1980). Measurements were made for 12 different wavelengths of light covering the range from 254 to 499 nm.

Strictly, the above method applies only to a monodispersion of droplets. If the droplet size distribution exhibits significant polydispersion, it is preferable to compute the theoretical transmittances corresponding to the predicted size distribution and compare these directly with the measured values. However, if the distribution is narrow (as is generally observed following spontaneous condensation) the measured extinction curve is almost identical to that produced by a monodispersion having a droplet radius equal to the Sauter mean value:

$$r_{32} = \int n(r) r^3 \, \mathrm{d}r \bigg/ \int n(r) r^2 \, \mathrm{d}r.$$

Optically determined droplet sizes are shown for the low and medium superheat tests in figures 16 and 17. It is clear that, even though full-sized blade profiles were used to generate droplets of a measureable size, all the droplets encountered were extremely fine. Typically, mean radii were in the range 0.04–0.08 µm (i.e. less than one quarter of the shortest available UV wavelength of 0.25 µm). Scattering of light by droplets of these magnitudes is very slight and the spectral curves obtained contain very little identifying structure. Moreover, in the case of the medium superheat tests, the wetness was also very low, thus compounding the difficulties. Under these conditions larger errors are inevitably incurred, as indicated by the estimated error bars included in the figures.

Nevertheless, the agreement between the calculated and measured droplet size is generally rather good, both in terms of absolute level and pitch-wise variation. Experimentally, this represents a considerable achievement since the droplet sizes involved are at the very limit of optical detection.

(i) *Low inlet superheat*

As shown in figure 16, the predicted Sauter mean droplet radii at low inlet superheat (tests L1, L2 and L3) exhibit considerable variation across the passage.

The large pitchwise variation in wetness fraction (figure 16*a*) is partly responsible for this effect, but it cannot account for all the observed variation because (for a given droplet number per unit mass of mixture) the droplet radius is proportional to only the cube root of the wetness fraction (see equation (4.1)). The more dominant factor is the total number of droplets formed during nucleation, which in turn is strongly influenced by the local expansion rate and by any interaction between the trailing edge shock wave system and the nucleation zone. An interesting example is shown in figure 16*b*, test L2, which is best explained with reference to the corresponding schlieren photograph and predicted pressure contours (figure 11).

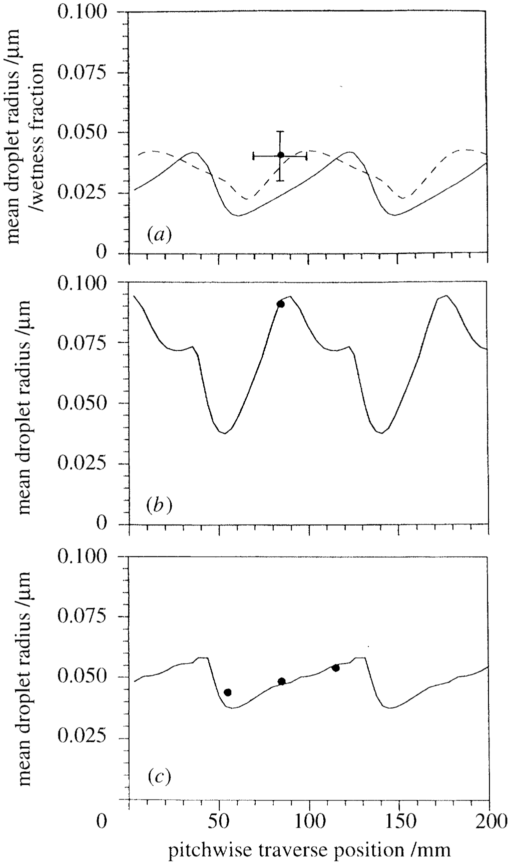

Figure 16. Comparison of predicted and measured downstream Sauter mean droplet radii for the low inlet superheat tests L1, L2 and L3: •, measured r_{32} (μm); ——, calculated r_{32} (μm); – – –, wetness fraction.

Near the suction surface, nucleation occurs in a region of quite rapid expansion, yielding a large number of small droplets. On the other hand, near the pressure surface the onset of condensation is delayed by the temperature rise through the trailing edge shock wave and occurs downstream in a region of low expansion rate, giving rise to fewer, but larger, droplets. At some point near the middle of the passage, the shock wave cuts through the nucleation zone, prematurely terminating the formation of embryos. This results in a particularly small number of droplets which consequently grow to a large size and are responsible for the peak in the predictions at midpassage. Unfortunately, only a single droplet size measurement was made in this test and so it is not possible to verify the predicted pitchwise radius variation. Clearly, it is very important to make more than just one droplet size measurement for each cascade experiment whenever possible.

(ii) *Medium inlet superheat*

The agreement between predicted and measured Sauter mean droplet radii is less good for the medium inlet superheat tests (M1, M2 and M3).

As shown in figure 17, the predictions fall outside the experimental error bars for three out of the five measurements. The most likely reason for this discrepancy

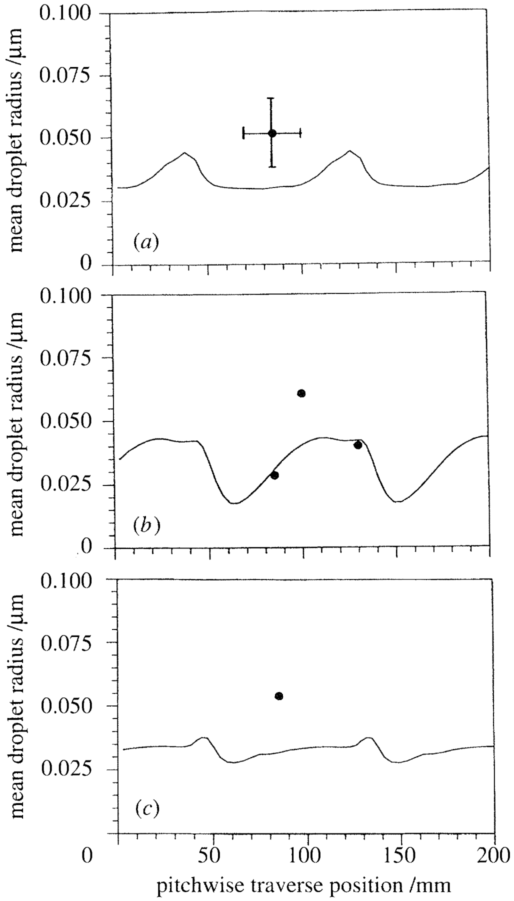

Figure 17. Comparison of predicted and measured downstream Sauter mean droplet radii for the medium inlet superheat tests M1, M2 and M3: ●, measured r_{32} (µm); ——, calculated r_{32} (µm).

is, once again, the inability of the calculations to accurately and crisply resolve the shock waves. As described above, the interaction of a shock wave with the onset of condensation can result in a prolonged nucleation zone and the production of a wide range of droplet sizes. Such polydispersions are: (i) very sensitive to the precise location of the shock waves; (ii) difficult to predict accurately using a numerical procedure which smears shock waves; and (iii) generate optical data which are difficult to interpret.

(d) *Loss measurements*

With the exception of the preliminary data of Skillings (1989), no measurements of loss due to irreversible condensation have been reported in the literature. This is a serious, although understandable, omission. Loss measurements are important, first to validate the theoretical basis of non-equilibrium calculations and second to establish whether the observed reductions in turbine stage efficiency can be accounted for by flow phenomena within a single fixed blade row, or whether they depend on interactions between the blade rows. It is also clearly of interest to compare blade

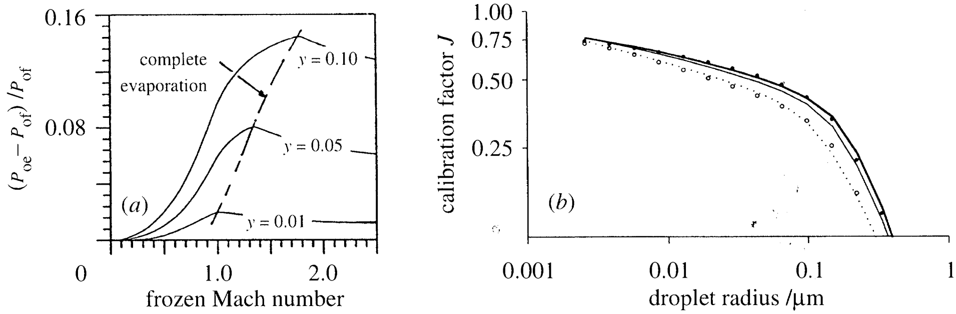

Figure 18. Interpretation of the Pitot probe measurements in wet steam: (*a*) comparison of equilibrium and frozen stagnation pressures; (*b*) calibration factor J as a function of droplet radius.

loss measurements for dry and condensing steam flows, both with each other and with numerical predictions.

(i) *Interpretation of Pitot probe measurements*

A major difficulty in obtaining accurate loss measurements in wet-steam flows is the interpretation of the Pitot pressure readings, for these are not directly related to the entropy increase across the cascade as for dry single-phase flow. The deceleration near the mouth of a probe is very rapid and the thermal and inertial relaxation processes may not proceed at a sufficient rate to maintain equilibrium conditions. Indeed, for large droplets the flow is effectively frozen with respect to the interphase transfer processes.

The possible range of pressures recorded by a Pitot probe therefore varies from the 'equilibrium value' $P_{0\mathrm{e}}$ (corresponding to the case where complete thermal and inertial equilibrium of the two-phase mixture is maintained throughout the deceleration) and the 'frozen value' $P_{0\mathrm{f}}$ (where interphase transfer processes are suspended). For a given equilibrium flow condition, both these stagnation states are well defined and can be calculated easily. Figure 18*a* shows curves of $(P_{0\mathrm{e}} - P_{0\mathrm{f}})/P_{0\mathrm{f}}$ plotted against the frozen Mach number of the flow approaching the probe (i.e. the Mach number based on the frozen speed of sound) for various wetness fractions. Obviously, the range of variation of $(P_{0\mathrm{e}} - P_{0\mathrm{f}})/P_{0\mathrm{f}}$ is of the same order of magnitude as the cascade loss itself and it is therefore absolutely essential to address the problem of probe measurement interpretation before any attempt is made to compute blade loss coefficients.

A theoretically based method for interpreting raw Pitot tube data has been devised by White & Young (1995) but the analysis is involved and cannot be presented here. The essential result is that the true 'frozen stagnation pressure' $P_{0\mathrm{f}}$ can be obtained from the raw probe measurement P_0 by application of the expression

$$\frac{P_0 - P_{0\mathrm{f}}}{\frac{1}{2}\rho_\infty u_\infty^2} = \frac{4y_\infty}{1 - y_\infty} J(r_\infty), \tag{6.1}$$

where $J(r_\infty)$ is the function of droplet radius shown in figure 18*b*.

(ii) *Traverse plane variations*

The discussion above has shown that values of both droplet size and wetness fraction are required to interpret the downstream traverse results. The droplet size is available from the optical measurements and the wetness fraction can be obtained

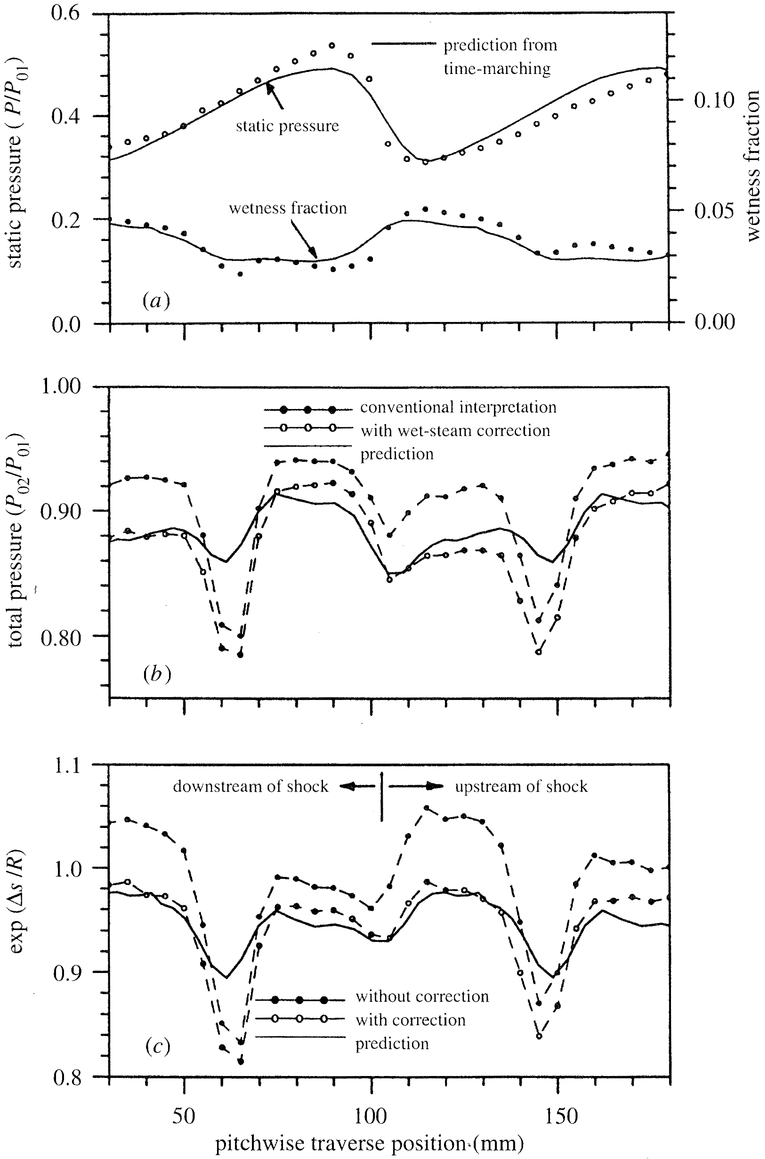

Figure 19. Comparison of measured and predicted downstream traverse results for test L1: (*a*) variation of static pressure and wetness fraction; (*b*) variation of total pressure ratio; (*c*) variation of entropy.

from the Pitot-static measurements if it is assumed that equilibrium is attained by the traverse plane. Making this assumption, the steady flow energy equation then gives

$$y_2 = (h_{g\text{sat}2} + \tfrac{1}{2}u_2^2 - h_{01})/h_{fg2}. \tag{6.2}$$

Figure 19*a* shows pitchwise variations at the traverse plane of static pressure and wetness fraction for test L1. For this case, the assumption that the flow has reached equilibrium is well justified and the agreement between prediction and measurement is very good. Particular points to note are that the static pressure measurements display good periodicity (despite the fact that there are only three passages) and that the pressure variation is well predicted by the time-marching calculations. The agreement between the predicted wetness fraction and the values calculated from equation (6.2) is also excellent. The steep changes in static pressure and wetness fraction near the middle of the passage are due to the intersection of the shock wave S_s with the traverse plane (figure 10).

Corrected and uncorrected Pitot pressures, also for test L1, are presented in figure 19*b*. For this case, the correction reduces the raw values by about 5%, bringing them into good agreement with the predictions in the central passage region. (Obviously, agreement is not to be expected in the wake regions since inviscid flow is assumed in the calculations.)

In contrast to single-phase flow, the stagnation pressure ratio across the cascade cannot be used directly as an indication of loss. For wet steam, it is necessary to compute the entropy change across the cascade from the total and static pressure readings. The entropy of the mixture is given by equation (4.5) and this can be calculated from the measured static pressure and the corrected total pressure if the flow is assumed to be in thermodynamic equilibrium at the traverse plane.

Calculated and 'measured' pitchwise variations in entropy for test L1 are shown in figure 19*c*. These are expressed non-dimensionally in the form $\exp(-\Delta s/R)$, where Δs is the increase in specific entropy above the cascade inlet value and R is the specific gas constant for steam. (For a perfect gas, $\exp(-\Delta s/R) = P_{02}/P_{01}$, and hence this representation aids comparison with conventional single-phase loss measurements.) It is evident from the figure that both the level and distribution of the true loss are quite different from that suggested by the uncorrected stagnation pressure ratios.

To emphasize the importance of correcting the Pitot pressures, it is worth noting that, if the measurements had been interpreted as for single-phase flow (i.e. accounting for the bow shock wave using $\gamma = 1.32$, but with no wet-steam correction), then the mean value of $\exp(-\Delta s/R)$ for test L1 would have been 0.912. If the flow had been treated as two-phase, but again with no account being taken of the thermal and inertial relaxation effects, the mean value of $\exp(-\Delta s/R)$ would have been 0.997 (with the entropy actually decreasing over much of the passage). Treating the flow as two-phase and applying the Pitot correction gives a mean value of 0.941, which agrees well with the predicted mean value of 0.946.

(iii) *Cascade loss coefficients*

The Markov energy loss coefficient ζ is defined in the conventional way as

$$\zeta = \frac{T_2 \Delta s}{\frac{1}{2} u_2^2}, \tag{6.3}$$

where all the quantities are 'mixed-out' values referred to a plane far downstream of the cascade. Mixing calculations were performed to relate the measured properties in the actual traverse plane with the required values in the fictitious far-downstream state.

Table 3 shows the 'measured' total mixed-out loss coefficients for all twelve cascade tests. Because of the experimental difficulties and the assumptions made in processing the data, great accuracy cannot be claimed for these figures. However, a careful study of table 3 does reveal plausible trends in the results. For example, with the exception of test H2 (where the flow was particularly far from equilibrium at the

Table 3. *Measured and calculated Markov loss coefficients*

	experimental Markov loss coefficients (%)					theory
test number	viscous loss	shock + wetness loss	mixing loss	total loss	shock + wetness + mixing loss	shock + wetness + mixing loss
L1	1.7	4.4	4.1	10.2	8.5	8.4
L2	1.8	5.6	1.5	8.9	7.1	6.6
L3	1.8	3.0	0.8	5.6	3.8	5.1
M1	2.9	4.1	2.8	9.8	6.9	6.3
M2	1.0	4.9	1.4	7.3	6.3	5.0
M3	2.5	2.3	1.0	5.8	3.3	4.3
H1	1.9	2.8	3.6	8.3	6.4	7.1
H2	1.1	3.0	2.2	6.3	5.2	4.6
H3	2.7	3.0	1.3	7.0	4.3	4.6
W1	1.9	3.6	2.8	8.3	6.4	8.0
W2	1.5	5.4	1.6	8.5	7.0	6.9
W3	2.2	3.0	1.0	6.2	4.0	5.1

traverse plane), the total loss coefficient increases with increasing exit Mach number for approximately constant inlet superheat. This behaviour is also found with cascade tests conducted in air.

It is also of interest to see how the losses are apportioned to the various loss generating mechanisms and to this end the measured Markov coefficients have been separated into three components as follows.

(i) Shockwave plus wetness loss—obtained from the mass-averaged values across a section of the traverse plane excluding the wake regions.

(ii) Viscous loss—obtained by subtracting the shock wave and wetness loss from the mass-averaged loss across the entire pitch at the traverse plane.

(iii) Mixing loss—obtained by subtracting the total mass-averaged loss at the traverse plane from the fully mixed-out loss.

Obviously this is a somewhat arbitrary decomposition, but the results, as shown in table 3, are both interesting and plausible. In particular, the magnitude of the thermodynamic wetness loss in comparison to the other losses is strikingly large. (The exit Mach numbers are low and hence the direct contribution of the shock waves themselves to the 'shock wave plus wetness loss' is very small indeed.)

By subtracting the 'viscous loss' from the measured total loss, it is possible to arrive at a figure which can, with some realism, be compared with the predictions of the time-marching calculations. These results are presented in the final two columns of table 3. Given the assumptions and data processing required, the agreement is quite remarkable: not only does the theory predict the correct trends but also the absolute magnitude of the loss to quite a respectable degree of accuracy.

In summary, although the results of this section cannot be said to provide definitive proof, all the evidence obtained indicates that the thermodynamic loss is predicted correctly by the theory.

7. Concluding remarks

The paper has described an experimental study of the non-equilibrium flow of condensing steam in a stationary cascade of turbine blades operating transonically. A detailed comparison of the experimental data with condensing flow theory was also undertaken using a two-dimensional inviscid time-marching computer program. Excellent agreement was obtained throughout and, on the evidence presented, it can be stated that the theory and calculation procedure reproduce accurately all the main features of steady transonic condensing flow in stationary cascades, including the complex interactions occurring between the trailing edge shock wave system and the regions of nucleation and rapid droplet growth.

By careful interpretation of the experimental data, it was possible, for the first time, to infer the loss due to irreversible condensation directly from experimental measurements. These results agreed well with the theoretical predictions and showed that the thermodynamic component of the total wetness loss in the nucleating stage of a steam turbine can be of comparable magnitude to the viscous profile loss.

No sign of periodically unsteady flow due to condensation (as is observed in converging–diverging nozzles with supercritical heat addition) was observed in the cascade but this does not preclude the possibility for other blade geometries.

Finally, the results presented in this paper demonstrate that the two-dimensional non-equilibrium theory and calculation procedures that have been developed will predict quantitatively the complex steam flows of transonic turbine blading. A fully three-dimensional non-equilibrium analysis for a multi-stage steam turbine is still a long way in the future but the work presented in this paper represents a step in that direction.

The computational work was performed at the Whittle Laboratory, Cambridge and the experimental work was carried out in the steam tunnel at the National Power Research Laboratories at Leatherhead. The authors are most grateful to the National Power Technology and Environmental Centre, Leatherhead (formerly the Central Electricity Research Laboratories) for sponsoring both aspects of the project. During the course of the work, A.J.W. was supported, initially, by a SERC CASE award (in collaboration with NPTEC), and subsequently by a grant from the Ford of Britain Fund of the Cambridge University Engineering Department. He is most grateful to both these sources of funding. The authors also thank Dr R. Jackson for his recommendations in the development of the time-marching program, Dr M. Hilditch for her design work on the cascade test section and Mr D. Reynolds and Mr M. Goodson for their technical assistance and help in acquiring the experimental data.

References

Bakhtar, F., Webb, R. A., Shojaee-Fard, M. H. & Siraj, M. A. 1993 An investigation of nucleating flows of steam in a cascade of turbine blading. *Trans. Am. Soc. Mech. Engrs: J. Fluids Engng* **115**, 128–134.

Bakhtar, F. & So, K. S. 1991 A study of nucleating flow of steam in a cascade of supersonic blading by the time-marching method. *Int. J. Heat Fluid Flow* **12**, 54–62.

Gostelow, J. P. 1984 *Cascade aerodynamics*. New York: Pergamon.

Gyarmathy, G. 1964 Bases for a theory for wet steam turbines. Bulletin 6 (CEGB Translation T-781) Institute for Thermal Turbomachines, Federal Technical University, Zurich.

Horlock, J. H. 1993 *Combined power plants*. New York: Pergamon.

Jameson, A., Schmidt, W. & Turkel, E. 1981 Numerical solution of the Euler equations by finite volume methods using Runge–Kutta time stepping schemes. *AIAA 14th Fluid and Plasma Dynamics Conf. (Palo Alto)*, paper no. 81-1259.

Lichtfuss, H.-I. & Starken, H. 1976 A critical review of the outlet flow of supersonic turbine nozzles. *Prace Instytutu Maszyn Przeplywowych (Trans. Instn Fluid Flow Machinery)*, Polish Academy of Science, **70–72**, 491–523.

Moore, M. J., Walters, P. T., Crane, R. I. & Davidson, B. J. 1973 Predicting the fog-drop size in wet steam turbines. *Instn Mech. Engnrs Conf. Wet Steam 4*, University of Warwick, paper no. C37/73.

Schnerr, G. & Dohrmann, U. 1988 Theoretical and experimental investigation of 2-D diabatic transonic and supersonic flowfields. *Symp. Transonicum III, IUTAM Symp. (Göttingen 1988)*, pp. 132–140. Berlin: Springer.

Sieverding, C. H. 1976 Unsteady flow measurements in straight cascades. *Proc. Symp. on Measuring Techniques in Transonic and Supersonic Cascades and Turbomachines (L'Ecole Polytechnique Fédérale de Lausanne, Lausanne 1976)* (ed. A. Bölcs & T. H. Fransson), pp. 73–82. Juris.

Skillings, S. A. 1989 Condensation phenomena in a turbine cascade. *J. Fluid Mech.* **200**, 409–424.

Walters, P. T. 1973 Optical measurement of water droplets in wet steam. *Instn. Mech. Engnrs Conf. (Warwick 1973)* paper no. C32/73. In *Wet Steam* **4**, 32–40.

Walters, P. T. 1980 Practical applications of inverting spectral turbidity data to provide aerosol size distributions. *Appl. Optics* **19**, 2353–2365.

Walters, P. T. 1985 Wetness and efficiency measurements in LP turbines with an optical probe as an aid to improving performance. *Joint ASME/IEEE Conf. on Power Generation (Milwaukee 1985)*, paper no. 85-JPGC-GT-9.

White, A. J. 1992 Condensation in steam turbine cascades. Ph.D. dissertation, Cambridge University Engineering Department.

White, A. J. & Young, J. B. 1993 Time-marching method for the prediction of two-dimensional, unsteady flows of condensing steam. *AIAA Jl Propuls. Power* **9**, 579–587.

White, A. J. & Young, J. B. 1995 Loss measurements and interpretation of Pitot pressures in two-phase vapour-droplet flow. *1st Int. Symp. on Two-phase Flow Modelling and Experimentation (Rome 1995)* (ed. G. P. Celato & R. K. Shah), vol. 1, 593–600.

Young, J. B. 1982 The spontaneous condensation of steam in supersonic nozzles. *PCH Phys.-Chem. Hydrodynam.* **3**, 57–82.

Young, J. B. 1984 Semi-analytical techniques for investigating thermal non-equilibrium effects in wet steam turbines, *Int. J. Heat Fluid Flow* **5**, 81–91.

Young, J. B. 1992 Two-dimensional, nonequilibrium, wet-steam calculations for nozzles and turbine cascades. *Trans. Am. Soc. Mech. Engrs: J. Turbomachinery* **114**, 569–579.

Received 15 December 1993; accepted 24 January 1995

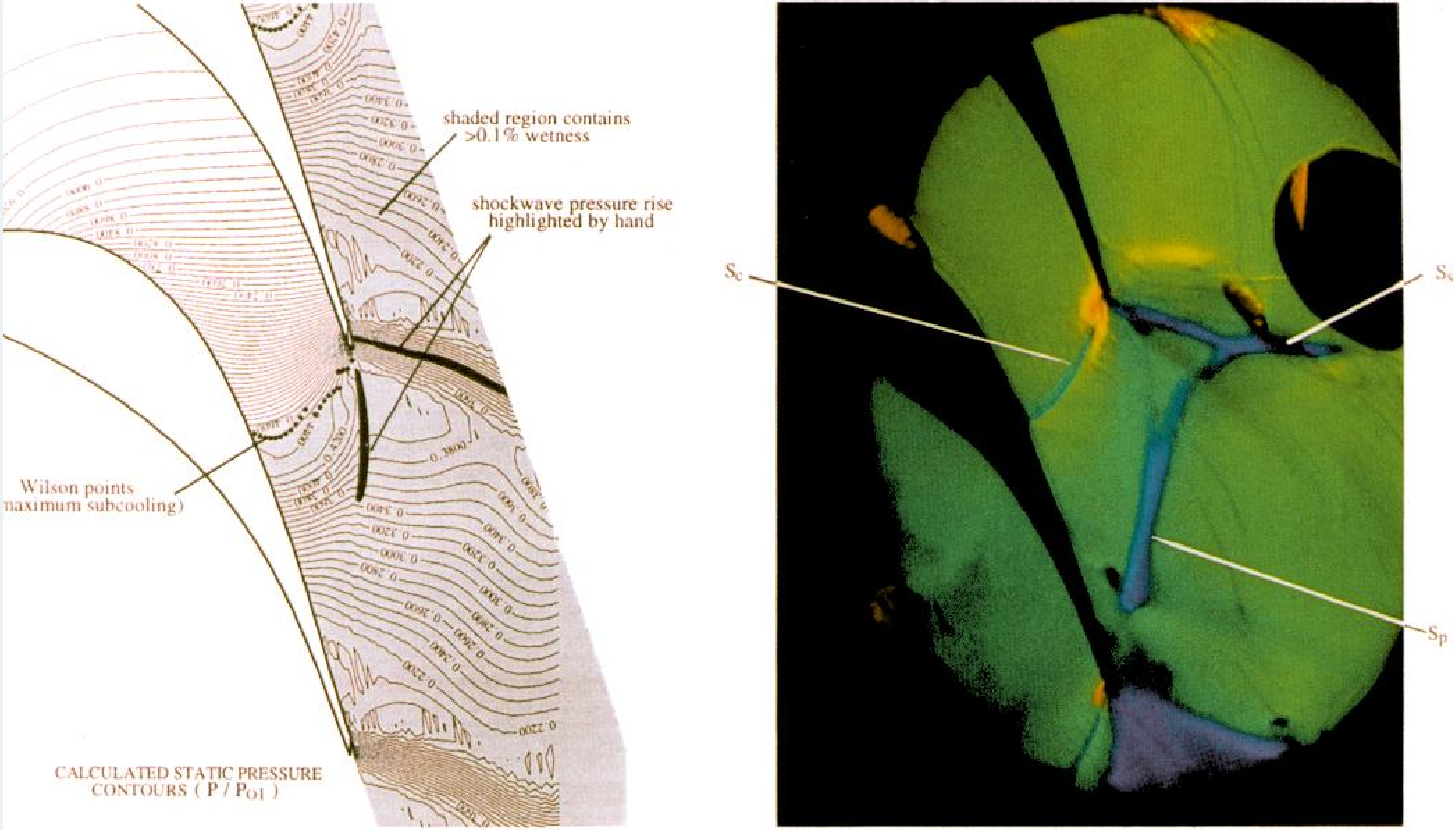

Figure 8. Test D1: dry inflow, $\Delta T_0 = 3.0\,^\circ$C, $M_{2s} = 1.5$, unconstrained exit flow.

PHILOSOPHICAL TRANSACTIONS OF THE ROYAL SOCIETY A MATHEMATICAL, PHYSICAL & ENGINEERING SCIENCES

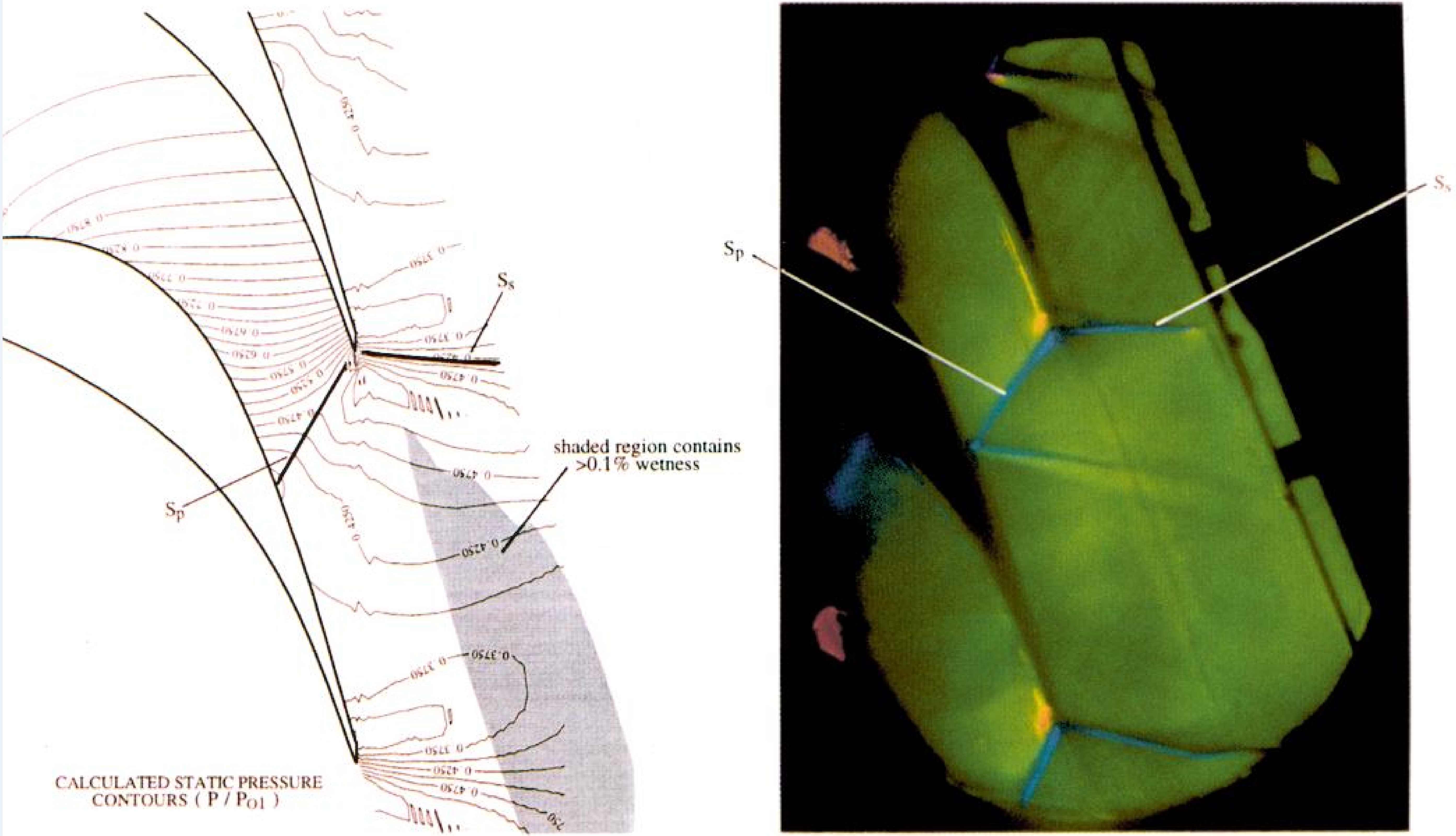

Figure 9. Test H2: dry inflow, $\Delta T_0 = 28.0\,^{\circ}\mathrm{C}$, $M_{2s} = 1.20$, porous tailboard.

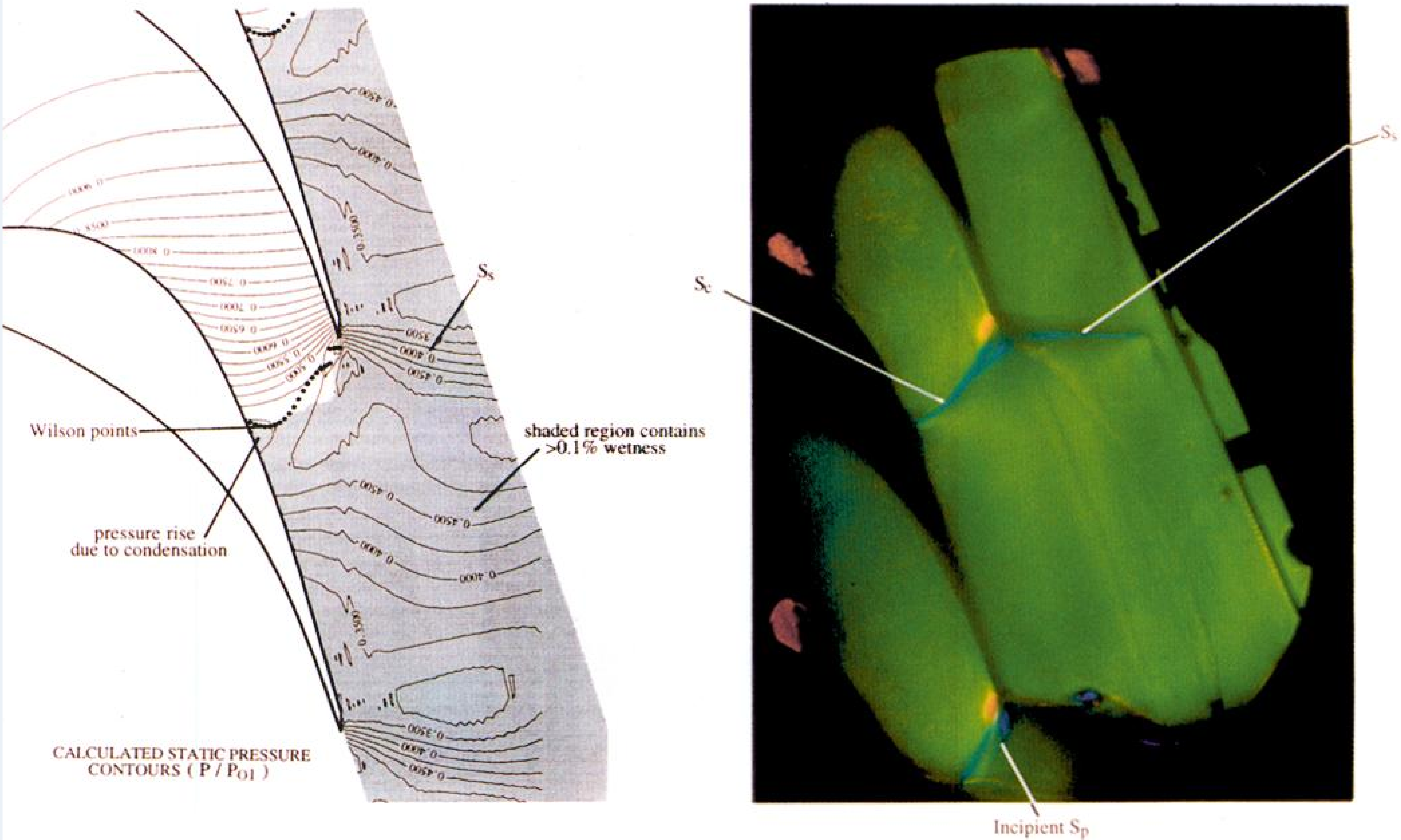

Figure 10. Test L1: dry inflow, $\Delta T_0 = 4.5\,^\circ\mathrm{C}$, $M_{2s} = 1.24$, porous tailboard.

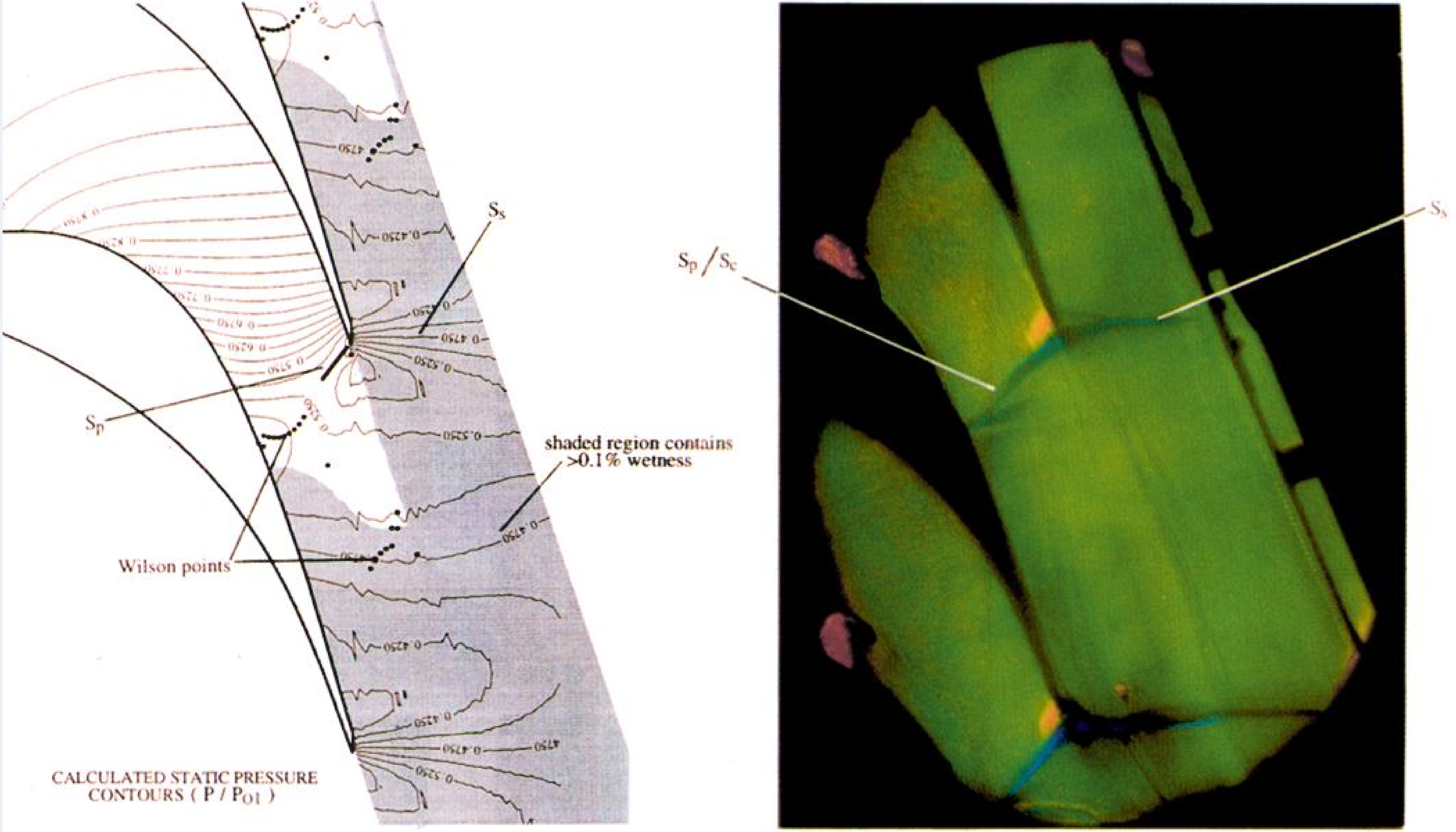

Figure 11. Test L2: dry inflow, $\Delta T_0 = 4.0\,^{\circ}\mathrm{C}$, $M_{2s} = 1.11$, porous tailboard.

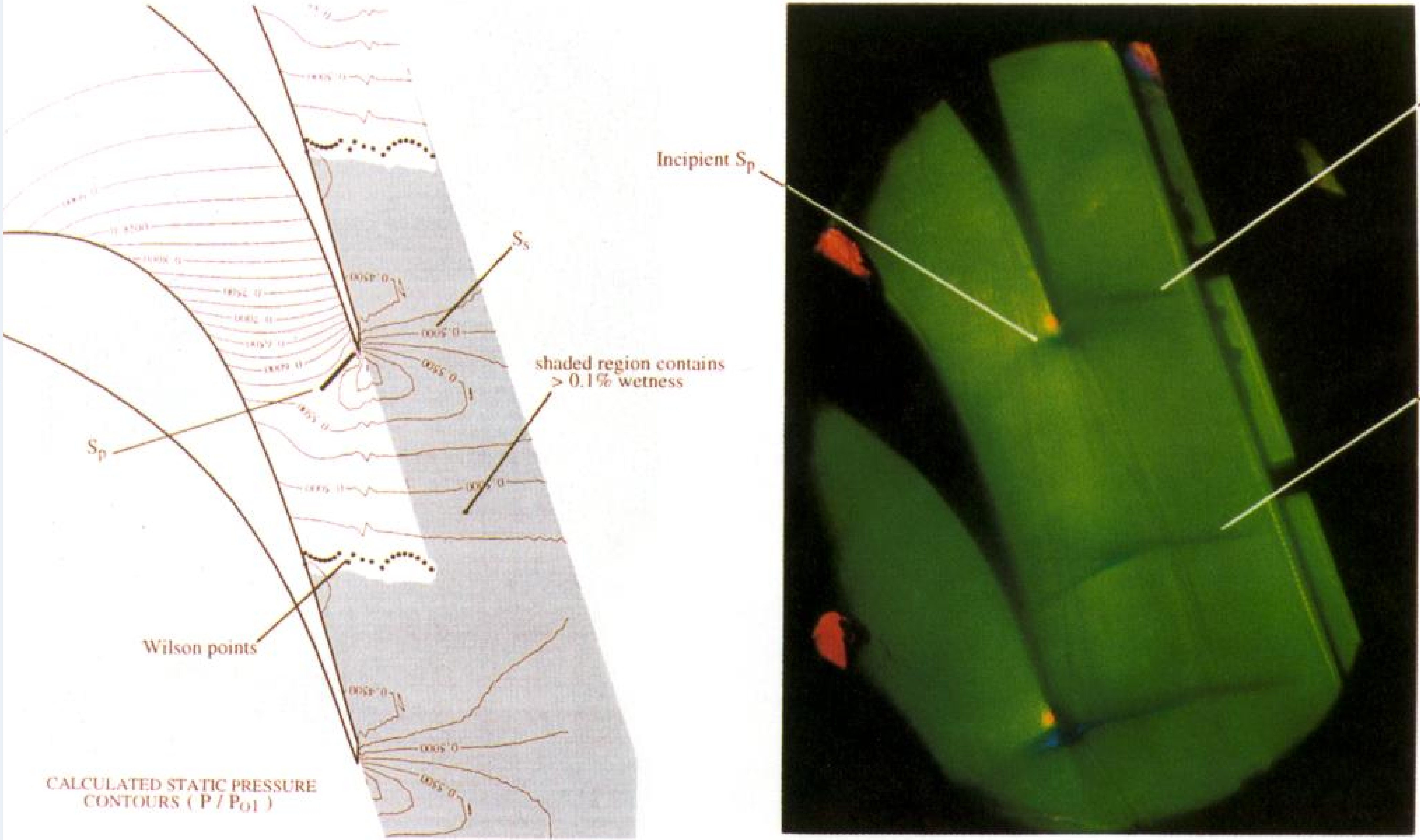

Figure 12. Test L3: dry inflow, $\Delta T_0 = 7.5\,^\circ\mathrm{C}$, $M_{2s} = 1.08$, porous tailboard.

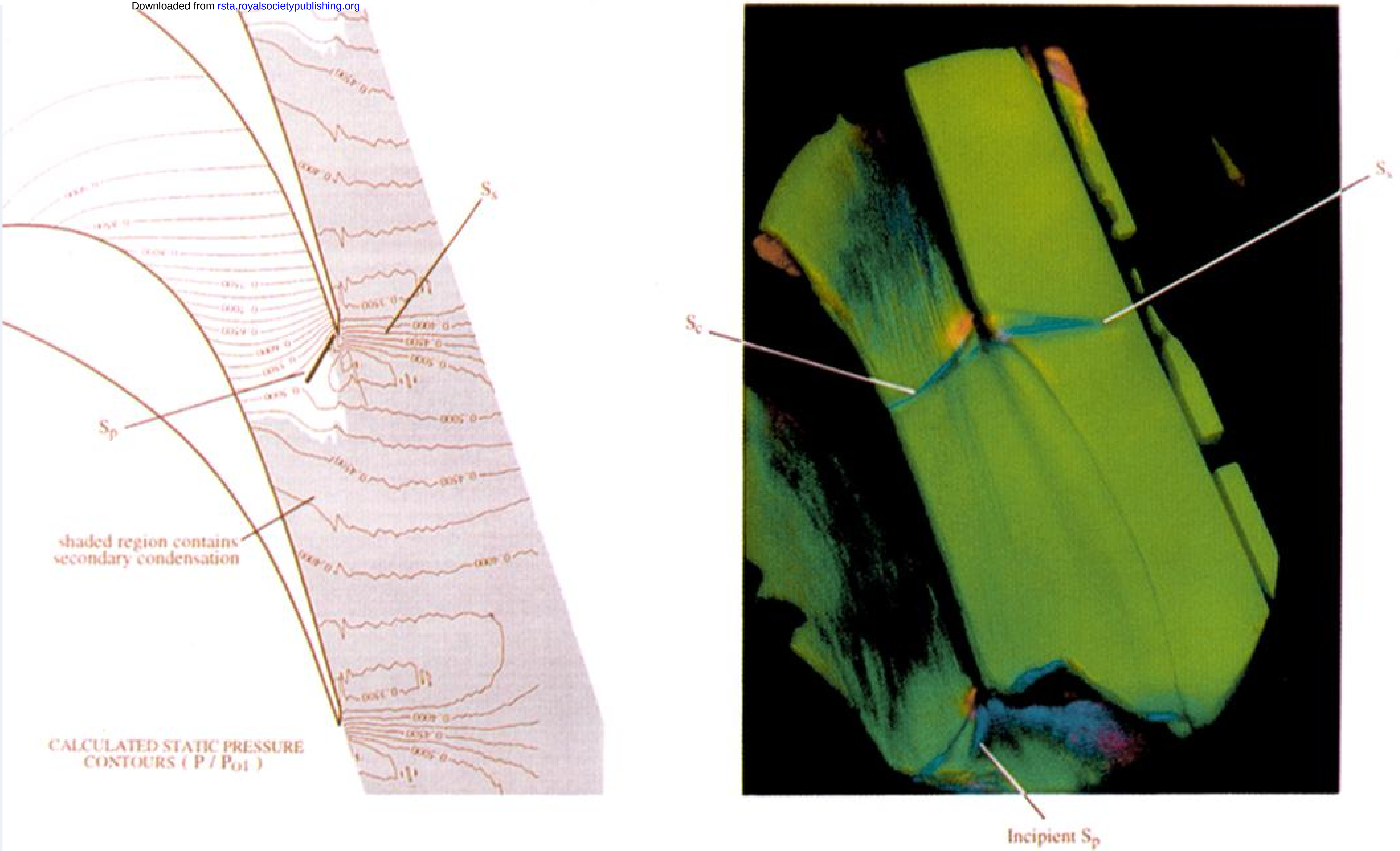

Figure 13. Test W1: wet inflow, $y_0 \approx 1.6\%$, $r_0 \approx 0.6$ µm, $M_{2s} = 1.20$, porous tailboard.